SANDIA REPORT

SAND2018-13911
Unlimited Release
Printed December 2018

Revisiting the Pipe Bomb V&V Problem using the BCJ Material Model

Kyle N. Karlson, Alexander A. Hanson, Bonnie R. Antoun

Prepared by
Sandia National Laboratories
Albuquerque, New Mexico 87185 and Livermore, California 94550

Sandia National Laboratories is a multimission laboratory managed and operated by National Technology and Engineering Solutions of Sandia, LLC., a wholly owned subsidiary of Honeywell International, Inc., for the U.S. Department of Energy's National Nuclear Security Administration under contract DE-NA0003525.

Sandia National Laboratories

Issued by Sandia National Laboratories, operated for the United States Department of Energy by National Technology and Engineering Solutions of Sandia, LLC.

Available to DOE and DOE contractors from
U.S. Department of Energy
Office of Scientific and Technical Information
P.O. Box 62
Oak Ridge, TN 37831

Telephone: (865) 576-8401
Facsimile: (865) 576-5728
E-Mail: reports@adonis.osti.gov
Online ordering: http://www.osti.gov/bridge

Available to the public from
U.S. Department of Commerce
National Technical Information Service
5285 Port Royal Rd
Springfield, VA 22161

Telephone: (800) 553-6847
Facsimile: (703) 605-6900
E-Mail: orders@ntis.fedworld.gov
Online ordering: http://www.ntis.gov/help/ordermethods.asp?loc=7-4-0#online

SAND2018-13911
Unlimited Release
Printed December 2018

Revisiting the Pipe Bomb V&V Problem using the BCJ Material Model

Kyle N. Karlson
Alexander A. Hanson
Bonnie R. Antoun

Abstract

For weapon safety assessments, Sandia has an interest in accurately predicting failure of pressure vessels at high temperature. In order to assess Sandia's predictive capability for these problems, a simplified validation problem for thermo-mechanical failure due to pressurization was developed and is referred to as the pipe bomb problem.[13, 14] In this study, several pipes were heated in a non-isothermal manner and pressurized until failure. The previous attempt to accurately predict the pipe bombs' failure pressures demonstrated a notable unconservative prediction. Due to this large bias in the simulation failure pressures toward higher pressures, we assumed that a mechanism driving failure or another aspect of the tests was missed in the original models. The goal of this work was to investigate potential sources of this bias focusing on geometric uncertainty and material model assumptions.

As with the previous work, our simulations of the pipe bomb experiments using the BCJ material model over predicted the failure pressures. While success cannot be claimed for the simulated failure pressures, we believe we accurately identified the remaining sources of error in the simulations. Specifically, the temperature mapping algorithm and the geometry are believed to be the primary contributors to the errors. As a result, future work should focus on improving the temperature mapping algorithm and consider using temperature fields determined by a calibrated thermal model that includes convection. Additionally, CT scans of remaining portions of the pipe bomb material inner diameter should be taken to further understand the variability this unmachined surface introduced to the pipe bomb specimens.

Figures

Tables

1 Introduction

For weapon safety assessments, Sandia has an interest in accurately predicting failure of pressure vessels at high temperature. In order to assess Sandia's predictive capability for these problems, a simplified validation problem for thermo-mechanical failure due to pressurization was developed and is referred to as the pipe bomb problem.[13, 14] In this study, several pipes were heated in a non-isothermal manner and pressurized until failure. The details of this previous work will not be described here; however, the previous attempt to accurately predict the pipe bombs' failure pressures demonstrated a notable unconservative prediction. In fact, the nominal predicted failure pressures for pipe bomb experiment PB1 were 38% higher than the experimental measurement and the predicted lower 0.025 percentile of the PB1 simulations (540-693 psi) was much higher than the experimental 0.025 percentile failure pressure (130 - 399 psi).[13] Due to this large bias in the simulation failure pressures toward higher pressures, we assumed that a mechanism driving failure or another aspect of the tests was missed in the original models. The goal of this work was to investigate potential sources of this bias.

Potential parameters influencing the failure pressure of the model include the pipe bomb temperatures, the numerics of the simulation, the material model assumptions, and the geometry. The previous work extensively validated their application of the measured temperatures from the experiments onto the model and determined their temperature mapping approach introduced errors of less than 5.9% to their predictions. As a result, we assumed that the temperature was not a likely source of the bias error. In terms of the simulation numerics, the previous work discusses not obtaining completed simulations with their fine meshes, but performed mesh convergence studies relying on assumptions based on the incomplete simulations. Due to these assumptions, they attribute a significant amount of uncertainty in their predictions to uncertainties in the mesh convergence study. We show that similar meshes with our model do demonstrate mesh convergence. As a result, we conclude that mesh discretization error is most likely not a major contributor to the bias error.

Therefore, for this effort, we investigate possible issues with the remaining areas of concern, material model assumptions and the geometry. The previous effort used the multilinear, elastic-plastic (MLEP) material model in SIERRA/Solid Mechanics (SierraSM) with temperature-dependent yield and hardening behavior.[16] A known phenomena exhibited by the 304L austenitic stainless steel from which the pipe bombs were machined is rate dependent plasticity behavior. The MLEP material model as used in the previous work neglects plasticity rate-dependence. Another potential area of concern is that MLEP is not history dependent. History-dependent plasticity may influence the solution to this problem since it first goes through a thermal strain driven buckling event before failing due to pressurization. The final material model assumption that may introduce error is MLEP's isotropic yield surface. The manufacturing process for extruded tubes can create microstructural texture anisotropy and elongated grains resulting in macroscopic material behavior anisotropy.[18, 17, 2] Although the previous work did incorporate geometry into their predictions, further investigation suggests that the initial measurements were over estimates of

the specimen wall thicknesses. As a result, we assess the influence of the pipe bomb wall thickness on the specimens' failure pressures.

To address the influence of material model assumptions, we simulate the pipe bomb with the BCJ and Hill Plasticity Damage material models. BCJ is an internal state variable material model incorporating temperature dependence, rate dependence and damage evolution. Specifically, we used the BCJ material model implemented as the DSA material model in SierraSM.[16] New tension data was obtained to influence calibration of the rate dependence parameters for BCJ. We also perform a preliminary investigation into yield anisotropy using the Hill Plasticity Damage. Although no new data was taken exploring plasticity anisotropy of the pipe bomb material, we assess the potential effect of anistoropic yield on the failure pressure of the models.

The original work focused on pipe bomb experiments PB1, PB2, PB4 and PB10. They focused on these experiments because they were similar enough to be considered repeat experiments. We will also focus on these experiments; however, we simulate the other experiments since most of the files to do so exist. The experiments we simulate are listed in Section 3 and Section 5.

2 Initial Material Model Calibration

The material model calibration effort focused on obtaining a quality fit to the data of interest from tension specimens extracted from the pipe bomb material. Specifically, the data of interest was low strain material behavior at low temperatures with an increasing concern for high strain behavior at high temperatures. The calibration process was performed for the BCJ material model using a hybrid calibration approach where results from a genetic algorithm optimization provided an initial point to a local pattern search optimization. The nominal BCJ material parameter set was then adapted to the Hill Plasticity Damage model without a re-calibration in an attempt to qualitatively assess the effect of anisotropy on the pipe bomb model failure pressure.

2.1 Original Material Characterization Data

During the original study, uniaxial tension tests were performed on the pipe bomb material for material characterization and material model calibration. The tests were performed at temperatures ranging from room temperature to 1073.15 K, and all tests were performed with a nominal engineering strain rate of 1e-3 $\frac{1}{s}$. At each temperature, several repeat experiments were run in an effort to quantify material variability. Figure 1 displays the experimental data from this material characterization work and Table 1 has the number of repeats taken for each temperature.

Table 1: Number of repeat experiments

Temperature (K)	296.15	373.15	473.15	673.15	873.15	973.15	1073.15
Number of Repeats	6	5	5	5	3	3	3

After this original set of tests, it was realized that rate dependence may play a role in failure of the pipe bomb. This is especially important because the pipe bomb fails primarily due to a structural instability during plastic deformation [15] and any strong rate dependence could affect how it fails. As a result, several additional high rate material characterization tests were performed at 973.15 K. Figure 2 shows the data from these tests and Table 2 shows the number of repeats for each test.

Table 2: Repeats of additional data at 973.15 K

Rate $\left(\frac{1}{s}\right)$	0.001	0.01	0.1
Number of Repeats	3	2	2

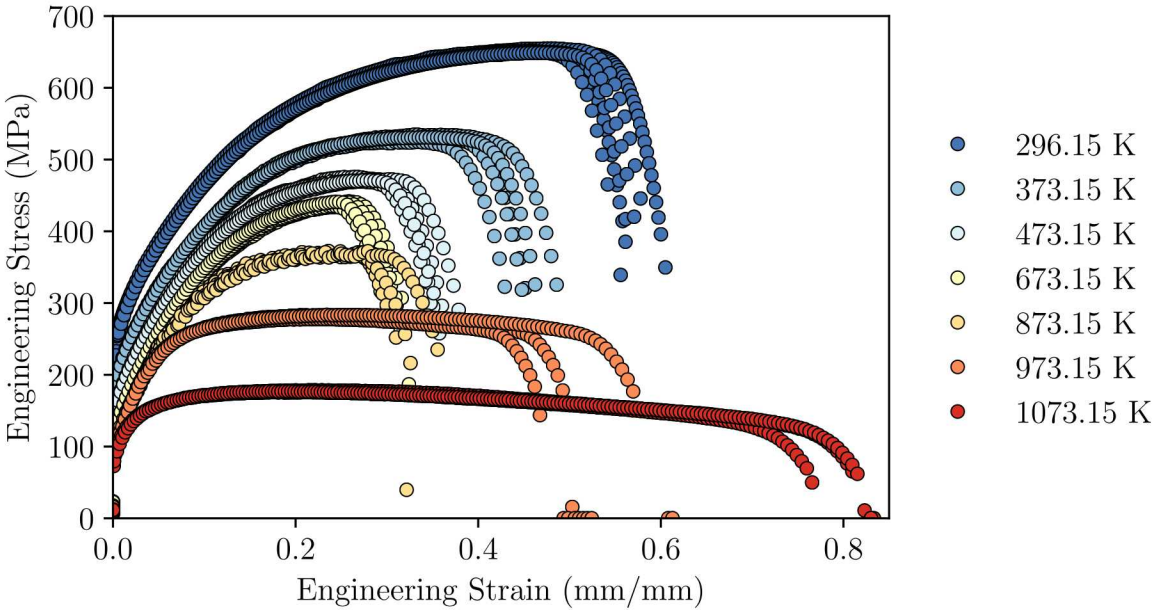

Figure 1: Original experimental data

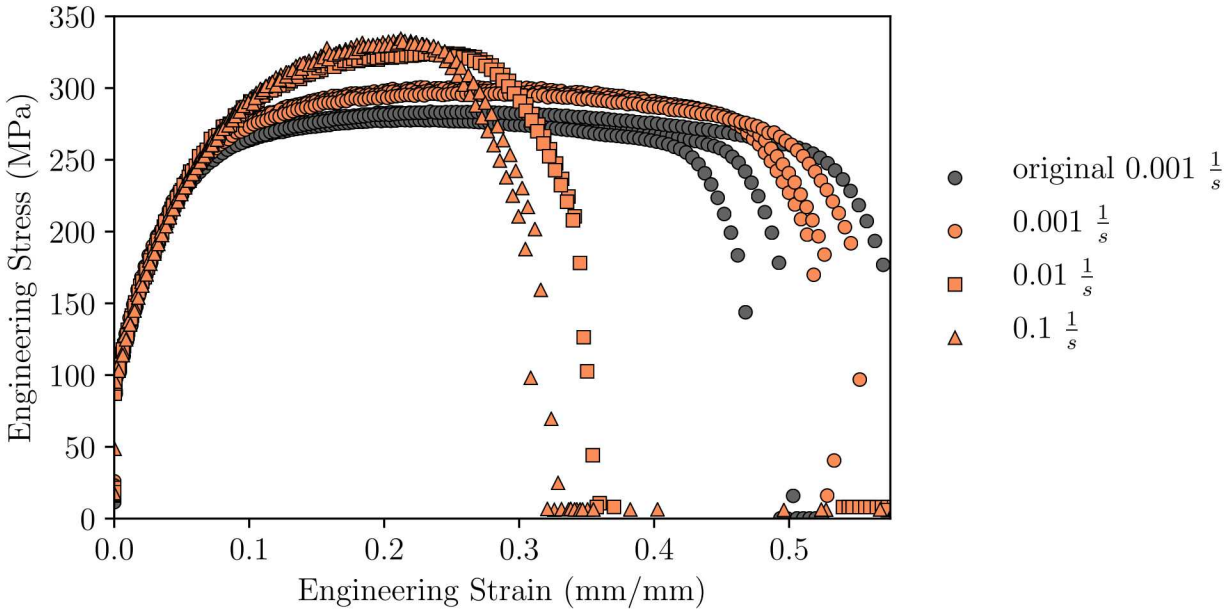

Figure 2: Additional high rate data at 973.15 K

2.2 BCJ Material Model

The details of the material model will not be described here as they can be found in the SierraSM manual under the BCJ_MEM material model section.[16] Note that we use a development material named DSA that is fundamentally the same as the BCJ material model and therefore, we will refer to the material model as the BCJ material model throughout the document. However, we did modify the material model with user prescribed temperature dependence functions for the yield stress, dynamic recovery, and static recovery. For the temperature dependent yield stress, we modified the BCJ function by adding Y_5 as a scale factor for $e^{(-Y_1/\theta)}$ in the denominator:

$$Y(\theta) = \frac{Y_0}{2\left(1 + Y_5 e^{(-Y_1/\theta)}\right)} \left[1 + \tanh\left(Y_2\left(Y_3 - \theta\right)\right)\right] \tag{1}$$

where Y_0, Y_1, Y_2, Y_3, and Y_5 are calibration parameters. For both the dynamic recovery(R_d) and static recovery parameters (Q_s and R_s), we used piece-wise linear temperature dependence in lieu of the Arrhenius-type temperature dependence specified in the BCJ model as it is not able to capture the desired behavior of those variables. The piece-wise linear temperature dependence of R_d was specified using a value at each temperature for which data exists, where as values of Q_s and R_s are specified only at the temperatures where static recovery is believed to be active, which includes temperatures above 873.15 K. For all other temperatures, Q_s and R_s are set zero which deactivates static recovery for those temperatures in the material model. We also note that the temperature dependence for any parameter in the BCJ material model can be prescribed using a Sierra function in the Sierra scope of the SierraSM input file. We use this capability for several of the material parameters during the initial material model calibration described in Section 2.3.

Additionally, a new rate dependence functional form was used in this study that differs from that in the SierraSM user manual. The rate dependence of the flow rule as written in the SierraSM user manual acts both on yield and the hardening behavior κ as shown by

$$\sigma_f = [Y + \kappa]\left\{1 + \sinh^{-1}\left[\left(\frac{\dot{\epsilon_p}}{f}\right)^{1/n}\right]\right\} \tag{2}$$

where f and n are the material parameters governing the material's rate dependence, and $\dot{\epsilon_p}$ is the material point equivalent plastic strain rate. Since sources [11] show that the hardening of 304L does not appear to be rate dependent, we used

$$\sigma_f = Y\left\{1 + \sinh^{-1}\left[\left(\frac{\dot{\epsilon_p}}{f}\right)^{1/n}\right]\right\} + \kappa \tag{3}$$

for the material model flow rule which only enables rate dependence on the material yield stress.

2.3 Initial Calibration

Initially a material model calibration was performed manually in order to obtain two sets of BCJ material parameters that matched the available data. The goal for the first parameter set was to match all data listed in Section 2.1 as closely as possible. Since BCJ allows for a large amount of flexibility in the temperature dependence of the material parameters, we found a set of parameters that fit the data well. Figure 3 shows the temperature dependence of select parameters from this calibration and Figure 4 shows the results of this calibration. It should be noted that these material parameters push the BCJ material model outside of its intended application space in an attempt to capture the dynamic strain aging exhibited by the material. This, in a way, is a misuse of the material model.

Dynamic strain aging manifests in the data as serrations in the load-displacement curve, inverted rate dependence (reduced strength with increased rate instead of the standard increase strength with increased rate), and lower strain-to-failure coupled with higher ultimate stresses.[4] All of these effects are present in the data and are most noticeable at temperatures 673.15 K and 873.15 K. However, we believe dynamic strain aging may be active at all temperatures from 373.15 - 973.15 K. Since SierraSM does not have a material model to simulate dynamic strain aging, we use the temperature dependence of the material model parameters to force the material model to match the data.

For the second calibration we chose to not match the data in the temperature range where we believe dynamic strain aging is active. Instead of attempting to force the model to match the data for these temperatures, we use the default BCJ temperature dependence functions to interpolate between 296.15 K and 1073.15 K or ignore temperature dependence all together for some parameters. A comparison between the first calibration and second calibration temperature dependence functions for select parameters are shown in Figure 3. Figure 5 shows the results from this calibration plotted against the relevant experimental data. Note that the higher rates were ignored for this calibration.

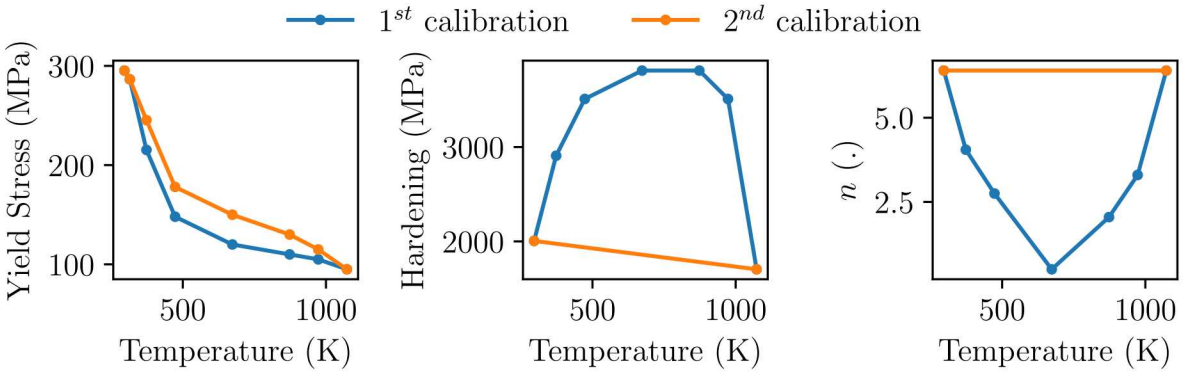

Figure 3: Comparisons of the two initial calibration's temperature dependence for yield, hardening and the rate dependence exponent n.

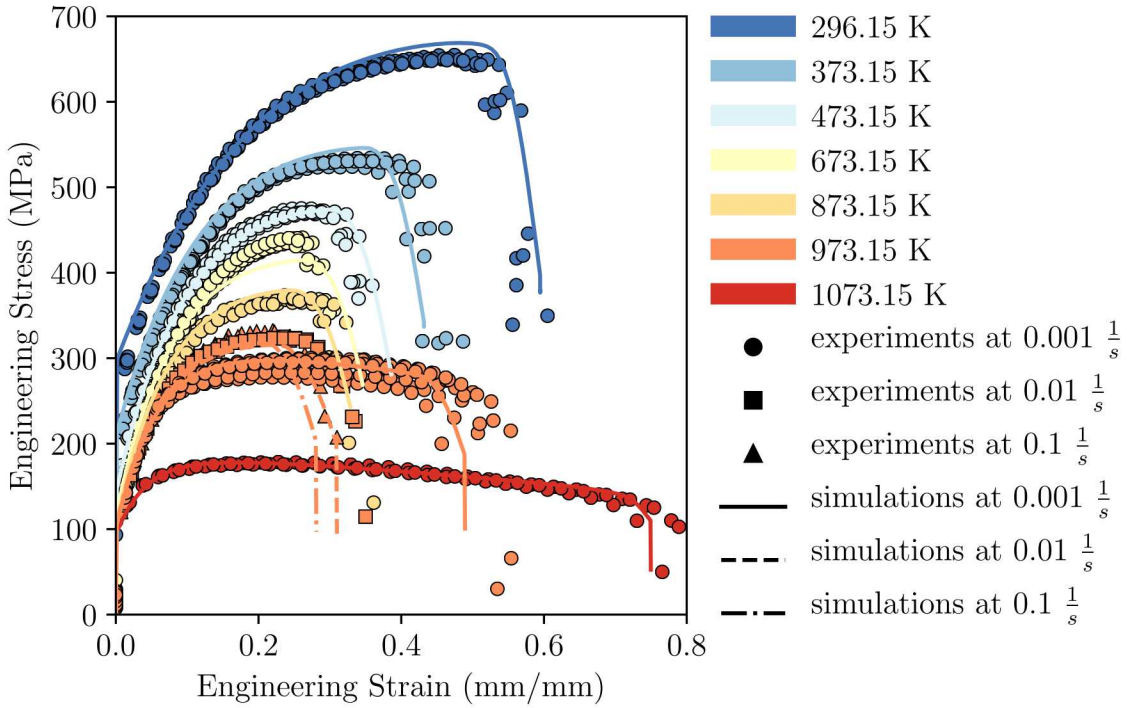

Figure 4: Results from the 1^{st} calibration

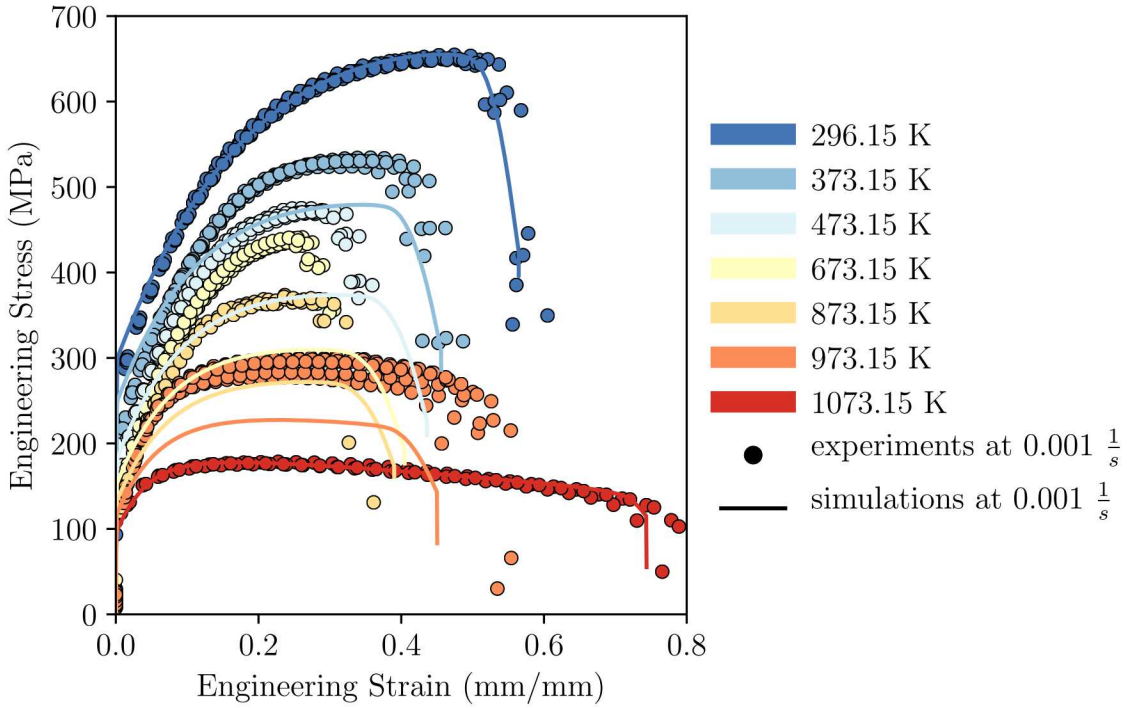

Figure 5: Results from the 2^{nd} calibration

In both of these calibrations, we added rate dependence to the material model yield stress. The rate dependence parameters were calibrated based on data from Nordberg[11]. For the first calibration, the rate dependence was significantly reduced at the mid-range temperatures due to dynamic strain aging. During the second calibration, the rate dependence was held constant. The two calibrations were developed as reasonable bounds on rate dependence for the pipe bomb material: the first calibration being the lower bound with less rate dependence and the second calibration being the upper bound with the more rate dependence. The goal was to use these two parameter sets to determine an upper and lower bound on the failure pressures for the pipe bomb model due to changes in rate dependence. Note that both these fits were possible due to the assumption that the literature data from Nordberg is valid for the pipe bomb material. Since this assumption may be incorrect, these simulations were only used for qualitative scoping simulations.

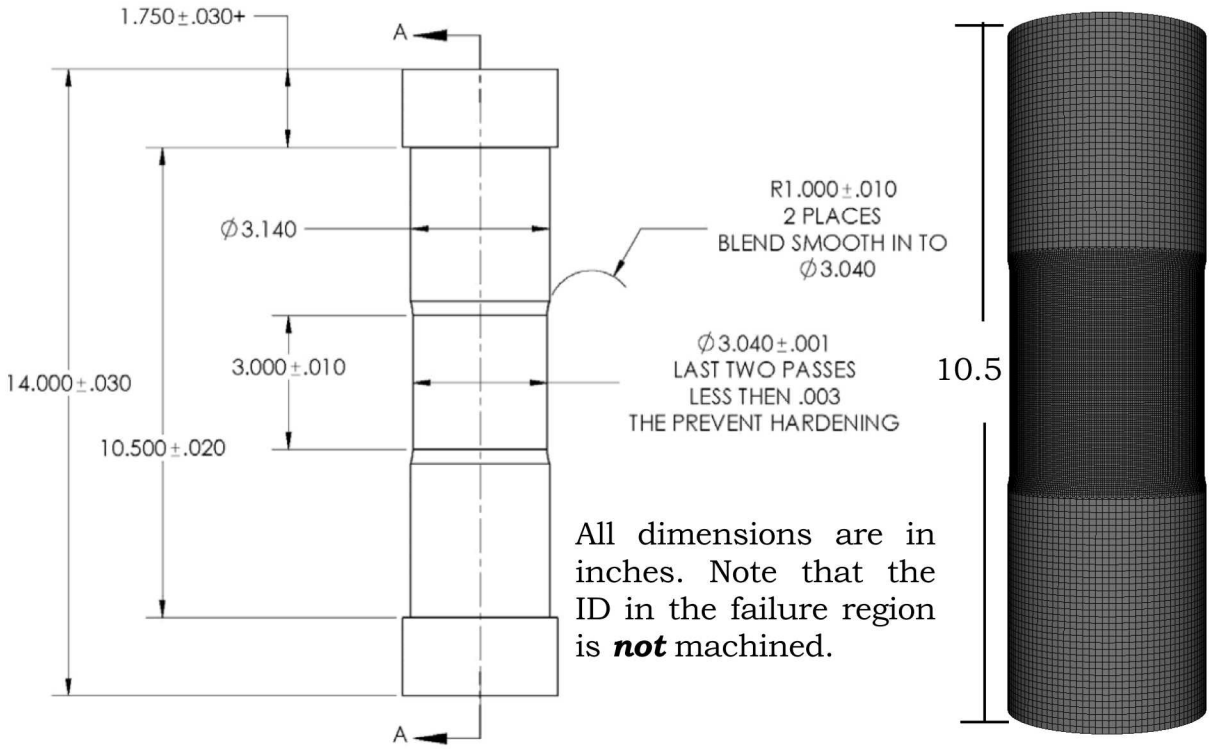

Figure 6: Comparison of the the pipe bomb model to the drawing. The ID is the ID of the 3 inch tube as produced. The pipe bomb model does not include the thick sections on the end. All other dimensions are equivalent.

3 Finite Element Model

The pipe bomb finite element model corresponded roughly to what was done in the previous work. We modeled the entire specimen; however, we did not include the thickest sections near the ends toward the grip. We assumed these sections were thick enough relative to the thinned down sections that they could be treated as rigid. Figure 6 compares the pipe bomb model to the drawing. For the boundary conditions, we applied the measured pressure history to the internal surface of the model and the measured grip displacement time histories were applied to the ends of the models in the axial direction. The displacements in the radial direction of both ends were fixed. The temperatures were applied using the same user-subroutine that was used for the previous work.[13, 14] However, a small change was added to this user-subroutine. A bug was found in the original subroutine that caused it to interpolate the temperatures to the nodes in the current configuration of the model. This bug was corrected so that the reference configuration coordinates were used for the application of the temperature field. Before the bug was corrected, the temperature field on the pipe bomb models became erratic as the pipe bomb deformed significantly before failure and moved outside of the validated space of the user subroutine. To account for differences in temperature, pressure, and end grip displacements, separate models for the specimens were created, each using the boundary conditions recorded from the corresponding test. We

chose to only model specimens PB1, PB2, PB4, PB8, PB9, PB10, PB15 and PB16 as the authors of the previous pipe bomb study had developed the temperature field interpolation subroutine only for these specimens.

Besides using BCJ, a few key model choices were different in our model than the previous work's model. For instance, we used total lagrange hex elements with volume averaging of the pressure instead of the uniform gradient elements in SierraSM. We have found that for failure problems these elements provide more reasonable solutions at a relatively small increase in computational expense. We also used implicit dynamics with the full tangent preconditioner. Implicit dynamics is required to solve this problem past its structural instability due to reasons related to what was said in Scherzinger's memo [15]. Another new SierraSM feature used was breach detect. Using breach detect, we were able to terminate the simulation as soon as a crack formed between the outside and inside surface of the model. We believe these changes to the finite element model were key to being able to obtain solutions reliably in less than 8 hours for our baseline mesh with 883,952 elements. The previous work mentions the models running for weeks without obtaining converged solutions. Our largest model during mesh refinement studies contained 7,003,744 elements, and ran to pipe bomb burst for the PB1 model within 44 hrs. Part of the successful completion of our simulations may be attributed to an issue with element death in SierraSM being corrected. However, for this problem we think the element death issue may not have been a problem due to the few elements that would need to be killed for the pipe bomb to breach.

The last notable difference is that our model used elements with an aspect ratio of approximately 1:4:4. The elements were thinner in the radial direction and larger in the axial and circumferential directions. This was required to keep the element count of the meshes more manageable since our baseline mesh had 6 elements through the 0.020" thick failure section. A mesh convergence study, documented in Section 5.1, was performed after the final material model calibration. Note that different element aspect ratios were not considered. Since the failure section's stress state very closely approximates plane stress and the failure is primarily driven by plasticity, fewer elements through the thickness with a 1:1:1 aspect ratio may have been sufficient.

All required model files are archived on Sandia's internal Gitlab server and are available at gitlab.sandia.gov.

4 Updating the Material Model Calibration

With the finite element model built and an initial material model calibration, we ran scoping simulations to determine the effect that adding rate dependence and ignoring dynamic strain aging would have on the pipe bomb model results. Initial results from the scoping simulations were promising and showed that the model ignoring dynamic strain aging failed earlier than the simulation with the material model calibration that strictly matched the data. As a result, this motivated additional testing to investigate the material behavior at specific strain rates and temperatures determined from the scoping simulations. The goal was to determine if dynamic strain aging was not active for the pipe bomb material when loaded with the strain rates and temperatures reported from the scoping simulations. Using the new data as a guide for material model choices, a final automated calibration was performed to available data. The calibrations were performed using MatCal [10], a wrapper for Dakota and SierraSM designed specifically for solid mechanics material model calibration.

4.1 Results from the Scoping Simulations and Additional Material Data Sets

As noted in Section 1, our study focuses on pipe bomb experiments PB1, PB2, PB4 and PB10. As a result, we ran the scoping simualtion using the PB10. The pipe bomb simulation of PB10 with the material model calibration from Figure 4 would not complete because the material model could not converge. This was somewhat expected due to the large variation of the rate dependence parameter n and the misuse of the material model. However, the simulation using the material model from Figure 5 did complete and predicted a failure pressure of 535 psi. In fact, all pipe bomb simulations using the material model ignoring dynamic strain aging predicted failure pressures with 25% error or lower when compared to their corresponding experiment. Table 3 lists the predicted failure pressures using the new material model parameter set ignoring dynamic strain aging. These favorable results motivated additional testing to verify the assumption that the pipe bomb problem exhibited material strain rates outside of those influenced by dynamic strain aging.

In order to determine the strain rates for the additional material characterization tests, we extracted detailed results from the PB10 simulation with the material model ignoring dynamic strain aging. Specifically, we plotted the plastic strain rate and temperature histories from elements near the failure region. Figure 7 and Figure 8 show the temperature and strain rate time histories extracted from the PB10 simulation, respectively. The results shows that for most of the simulation, the elements are experiencing plastic strain rates either well below or well above the nominal strain rate of 1e-3.

As a result, we performed additional testing at the higher temperatures (673.15 K, 873.15 K, and 973.15 K) and at strain rates ranging from 1e-5 $\frac{1}{s}$ to 1 $\frac{1}{s}$. The plastic strain rate limit at 1 $\frac{1}{s}$ was due to limits imposed by the load frame that could support high temperature testing. The low-end plastic strain rate limit was due to the length of the test being over

Table 3: Predictions for pipe bomb failure pressures with material model calibration ignoring dynamic strain aging

Specimen	**Simulated Failure Pressure (psi)**	**Experiment Failure Pressure (psi)**	**% error**
PB1	491.1	605.5	-18.9
PB2	529.4	587	-9.8
PB4	492.9	655.2	-24.7
PB8	567.0	637.5	-11.1
PB9	731.3	732	-0.1
PB10	535.8	647	-17.2
PB15	585.1	633.7	-7.7
PB16	588.4	637.3	-7.7

the length of the work day. The results from these tests at 673.15 K and 873.15 K are shown in Figure 9 and Figure 10, respectively. An additional test was run at 973.15 K with a strain rate of 1 $\frac{1}{s}$. This experiment had a similar engineering stress-strain curve as the 0.1 $\frac{1}{s}$ engineering stress-strain curve shown in Figure 2 and was not plotted here for brevity.

These results suggest that dynamic strain aging cannot be ignored. We come to this conclusion because for the rates greater than 1e-3 $\frac{1}{s}$, the material mechanical behavior does not change significantly. In fact, for all rates at the higher temperatures the yield stress for the material remains approximately the same. This is most likely due to dynamic strain aging inhibiting the rate dependence of the material. It is important to note that at lower rates the data show that a different form of rate dependence is evident for the temperatures above 673.15 K. Due to the low strain rates and high temperatures, the observed softening of the material could be due to static recovery or re-crystallization.

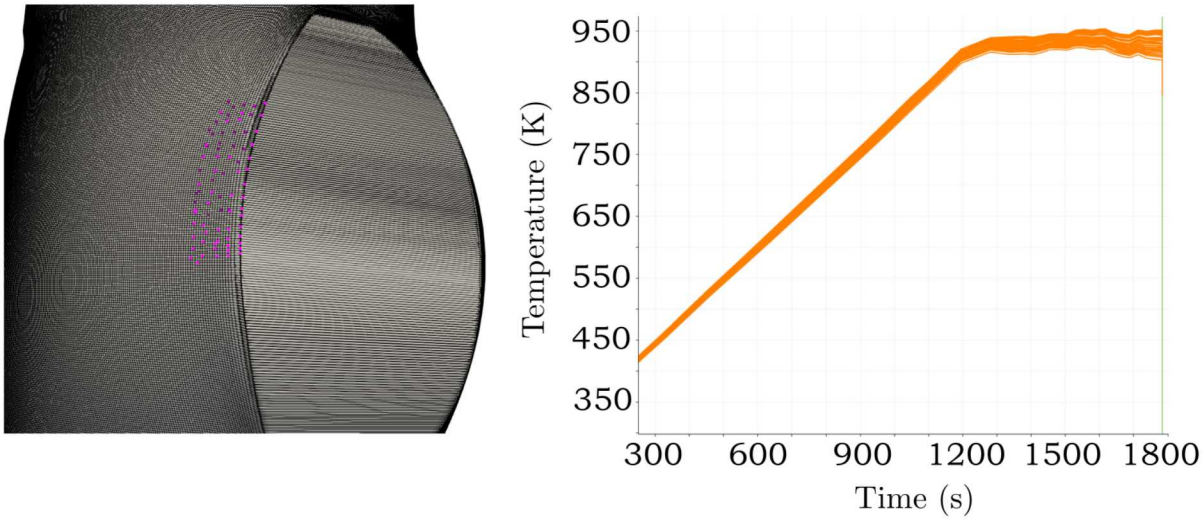

Figure 7: Expected temperatures in the region of failure from the PB10 simulation using the material model ignoring dynamic strain aging. The image on the left shows where these temperatures were extracted from.

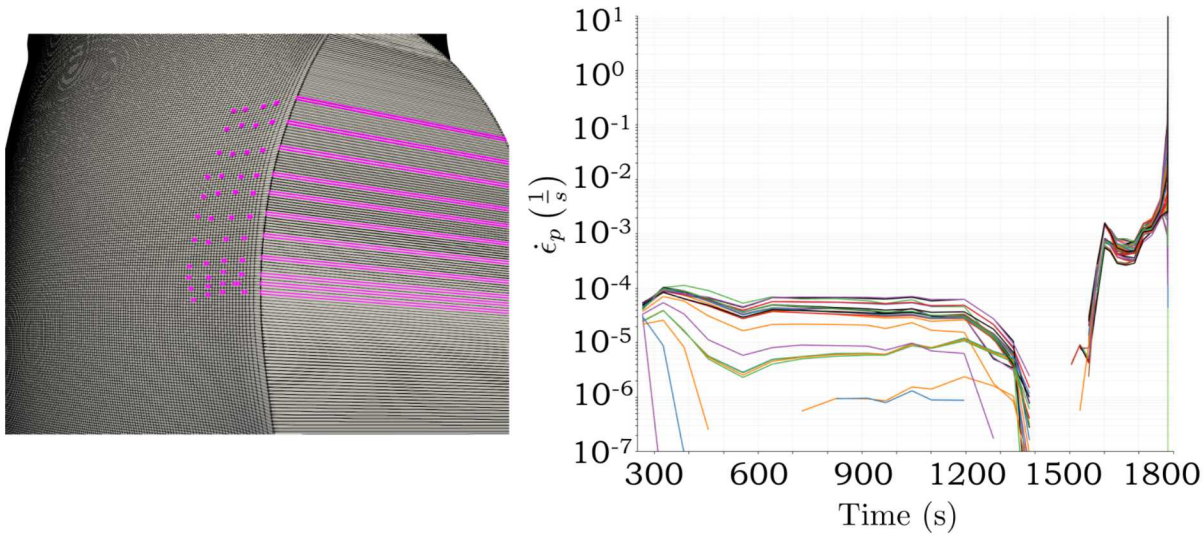

Figure 8: Expected plastic strain rates in the region of failure from the PB10 simulation using the material model ignoring dynamic strain aging. The image on the left shows where these strain rates were extracted from.

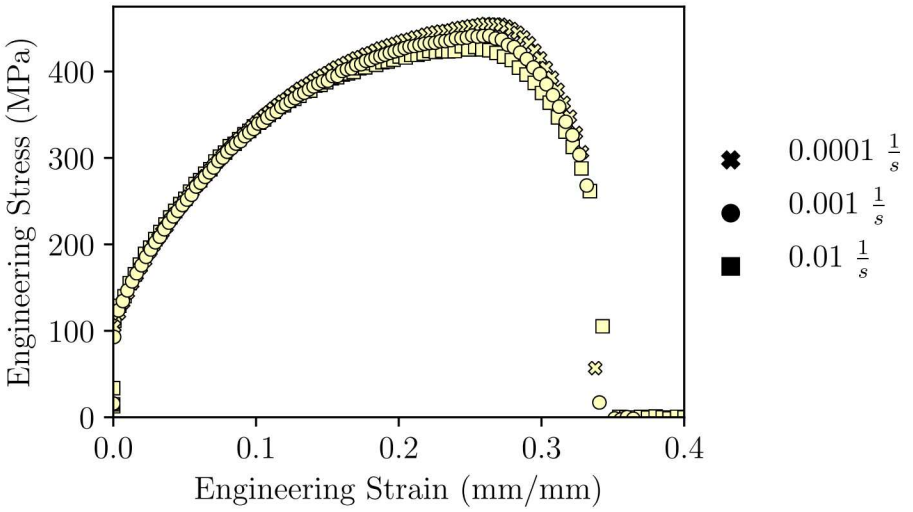

Figure 9: Additional material characterization data at 673.15 K

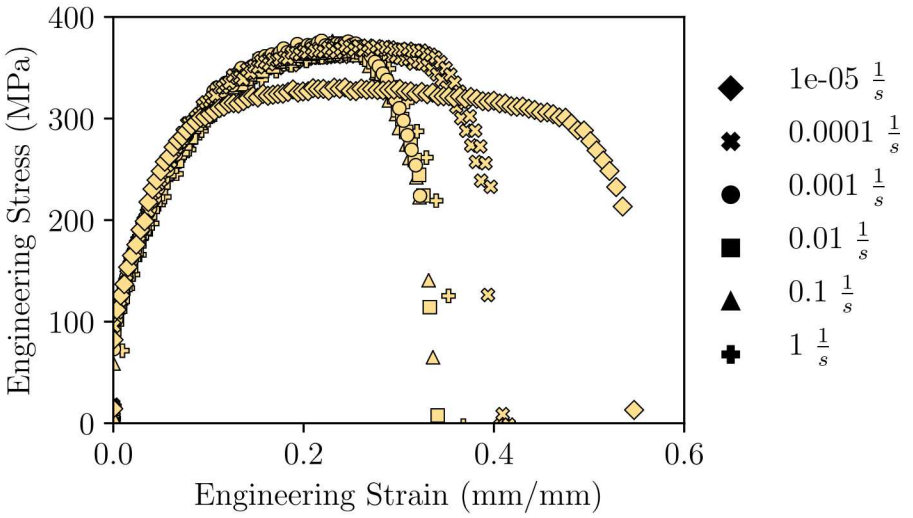

Figure 10: Additional material characterization data at 873.15 K

4.2 Hybrid Calibration Approach

Although our initial hypothesis was proven incorrect, we moved forward with a final material calibration including only the low-rate, rate dependence. We chose to use the static recovery terms of the BCJ material model to simulate this low-rate behavior and make the flow rule rate dependence terms f and n negligible. Since the experiments listed in Section 4.1 were being performed near the end of this work, the data was not explicitly used in most of the calibrations. However, the insights on the pipe bomb material behavior gained by reviewing the results from the experiments as they completed were used to guide material modeling choices. Additional guidance on the calibration was gained by using the scoping simulations to show that only the high temperatures needed a quality material model fit at high strain. The scoping simulations for the pipe bomb simualtions of interest (PB1, PB2, PB4, and PB10) showed that elements with temperatures less than 873.15 were not strained above 20% engineering strain. As a result of these realizations, the material modeling choices for the new calibration were to (1) disable rate dependence at rates above 1e-2 $\frac{1}{s}$, (2) only calibrate to strains up to 20% engineering strain for temperatures below 873.15 K and (3) to use the static recovery terms in BCJ to model rate dependence below 1e-2 $\frac{1}{s}$.

This final calibration included two steps: (1) a global calibration using SOGA (a genetic algorithm in Dakota), and (2) a local pattern search method (Dakota's mesh adaptive search algorithm). Although not detailed here, a large amount of work went into deciding the appropriate temperature dependence to use for the BJC material parameters. The success of the calibration was strongly dependent on these functional forms and the bounds for the material parameters feeding into these temperature dependence functions. Through a combination of sensitivity studies and guided simulations/calculations, the temperature dependence functions listed in Section 2.2 and the bounds listed in Table 4 were determined for the global calibration using SOGA. Note that the parameter Q_s was calibrated on a log scale. The objective function was the error between the simulated engineering stress-strain curves and the experimental data. The higher temperature results were weighted more heavily than the low temperature results, and the data at strains above 20% engineering strain for temperatures below 873.15 K were weighted near zero. The algorithm converged after 214 generations and required 28,507 objective function evaluations. The results from this step of the calibration are shown in Figure 11. Figure 12 and Figure 13 show the material model calibration results for only temperature 893.15 K and temperature 973.15 K, respectively. Note that we did not calibrate to data at 1073.15 K because the pipe bomb specimens of concern (PB1, PB2, PB4 and PB10) did not experience temperatures significantly higher than 973.15 K. The calibrated material model file is included in Appendex C.1.

A final validation step of the calibration was performed by comparing the tension specimen gage section profiles of the simulation results at 973.15 K to experimentally measured profiles for several rates. Figure 14 shows these profile comparisons. The simulation results compare well for the rates above 1e-3 $\frac{1}{s}$ and exhibit larger error for slower rates. This is expected due to the model form error discussed in the previous paragraph. Overall, this validation exercise improved our confidence in using the static recovery terms in BCJ to account for

Table 4: Material model parameter bounds and results for the global calibration using SOGA.

Model Parameter	**Lower Bound**	**Upper Bound**	**Calibrated Value**
Y_0 (MPa)	350	600	575.8
Y_1 (K)	350	600	472.7
Y_5 (.)	4	8	6.3
H (MPa)	2500	4500	3526.2
R_d^{296}	0	10	4.0
R_d^{373}	0	10	5.2
R_d^{473}	0	10	5.9
R_d^{676}	0	15	6.8
R_d^{873}	0	15	7.8
R_d^{973}	0	15	9.1
Q_s	10^{-13}	10^{-12}	$10^{-12.47}$
R_s	40	70	53.8

the observed rate dependence in the experimental engineering-stress strain curves. Model form error related to our use of static recovery is evident in Figures 12 and 13 primarily in the strain-to-failure and the stress at higher strains at low-rates. The errors are relatively small and the optimization algorithms could not improve the simulation results.

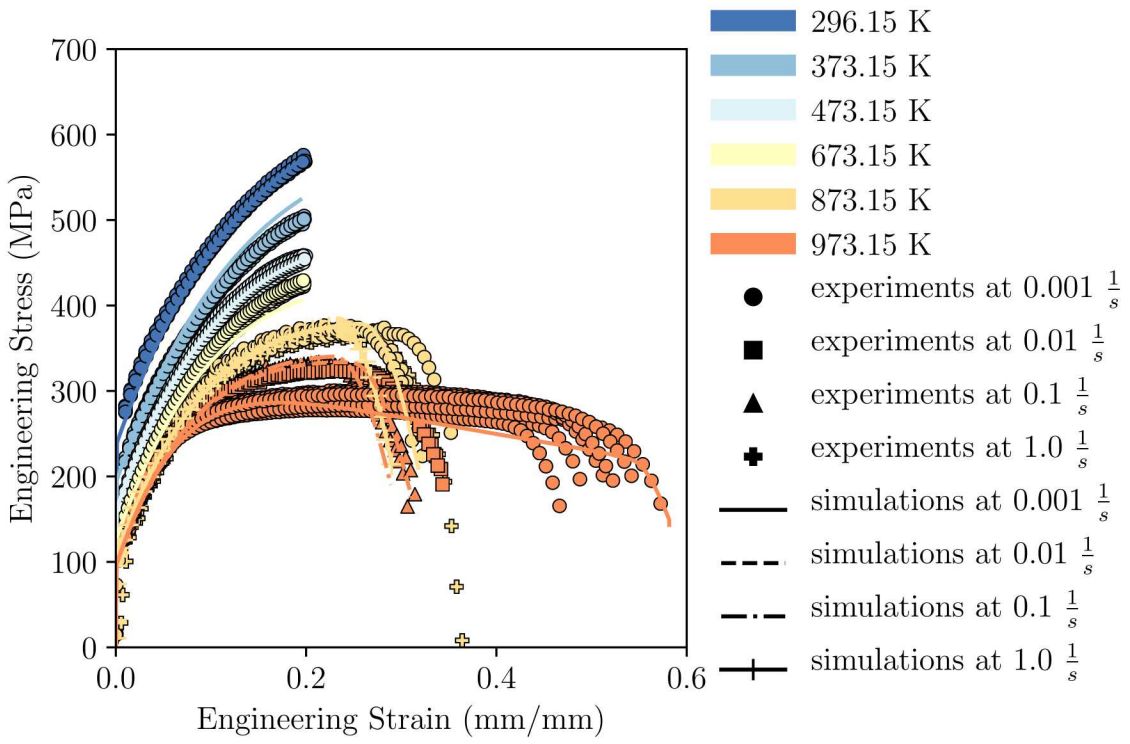

Figure 11: Results from the global calibration using SOGA plotted against the experimental data.

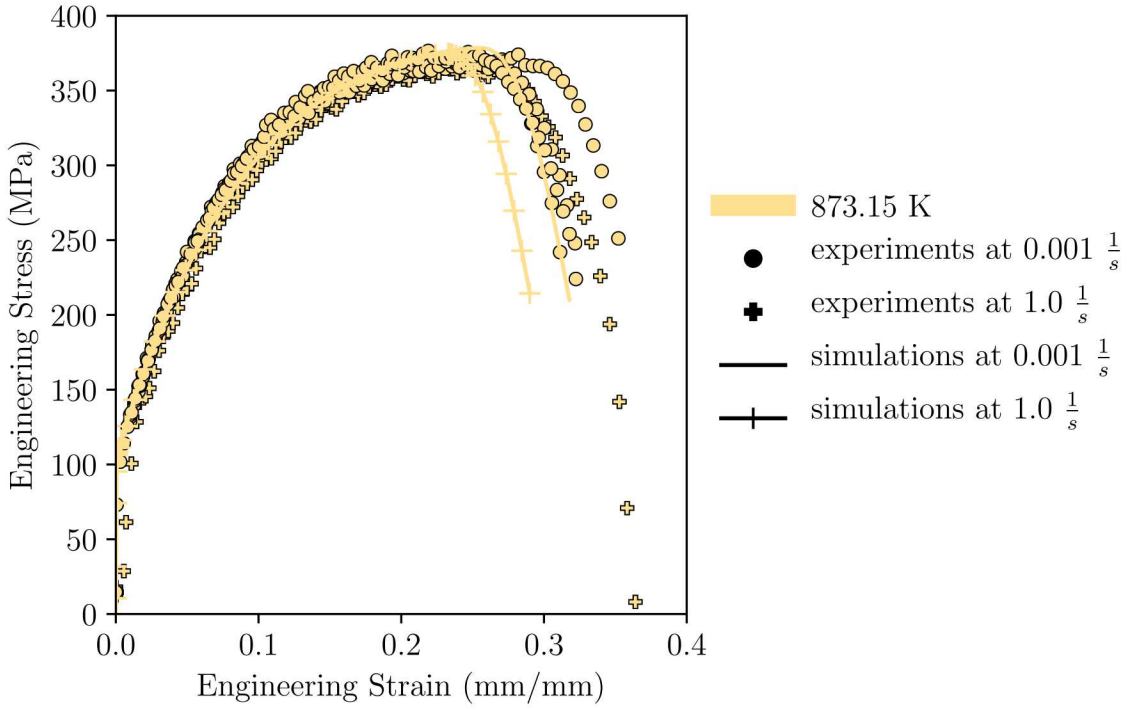

Figure 12: Results from the global calibration using SOGA plotted against the experimental data for temperature 873.15 K.

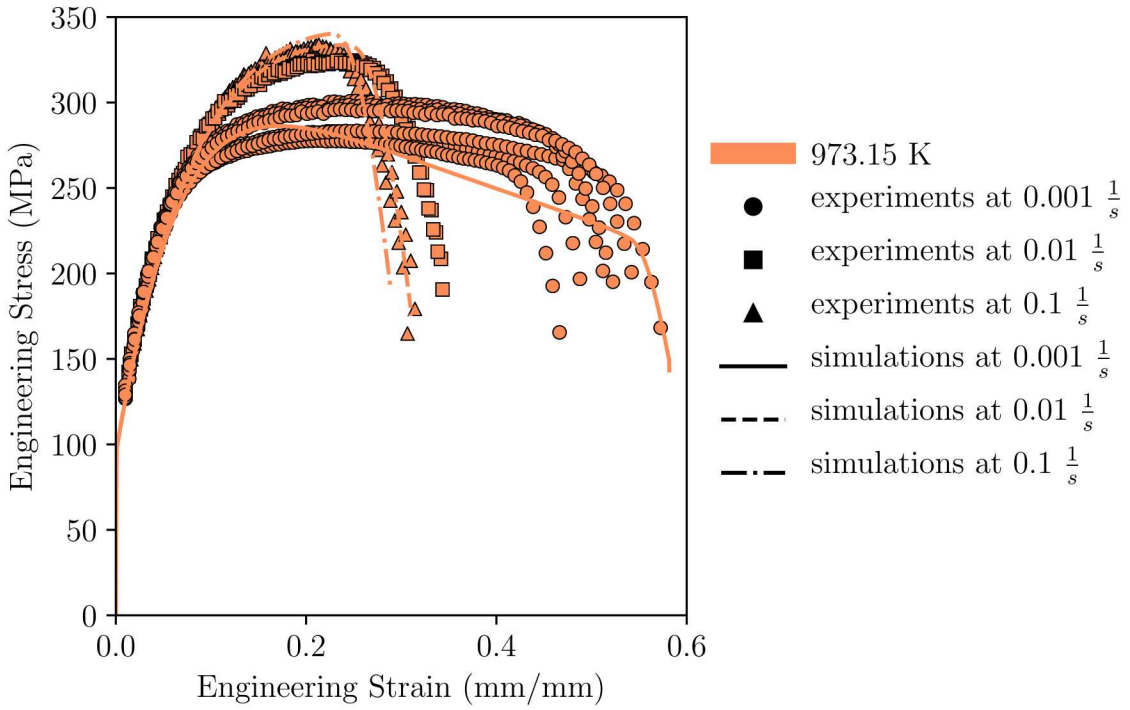

Figure 13: Results from the global calibration using SOGA plotted against the experimental data for temperature 973.15 K.

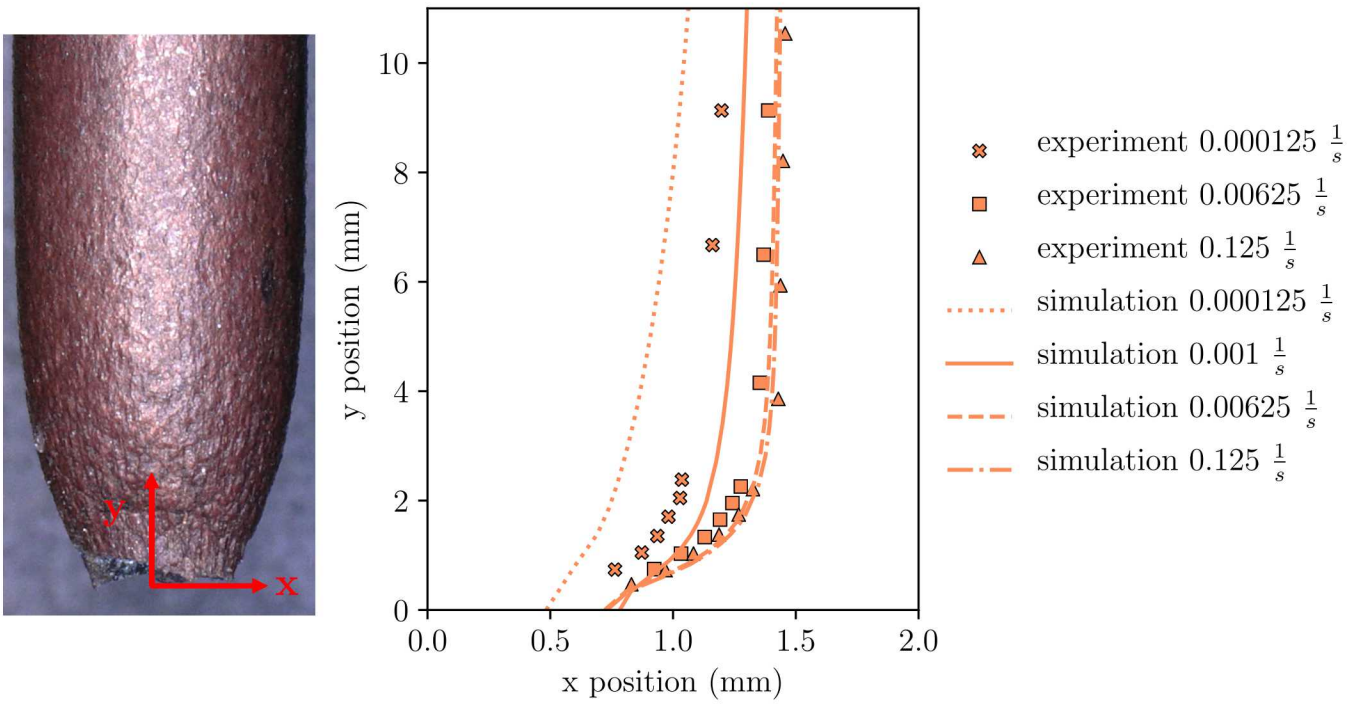

Figure 14: Tension specimen gage section profiles from the global calibration using SOGA plotted against experimental data for temperature 973.15 K. The experimental image to the left shows the failed gage section profile of the specimen tested at rate 0.125 $\frac{1}{s}$.

After the global calibration finished, a local calibration was performed to get find the new local minimum after re-sampling the data sets using bootstrapping. The bootstrapping method and results from the uncertainty quantification activities are described in Section 7.1. Several local derivative-free algorithms were assessed on this calibration problem, and coliny pattern search returned the lowest objective function value on the calibration to the original experimental data sets. However, due to the design of the coliny pattern search algorithm, it tended to return the exact same parameter values for calibrations with different bootstrapping samples of the experimental data. As a result, mesh adaptive search was used for the uncertainty analysis calibrations as it tended to return unique parameter sets for each bootstrapping sample set.

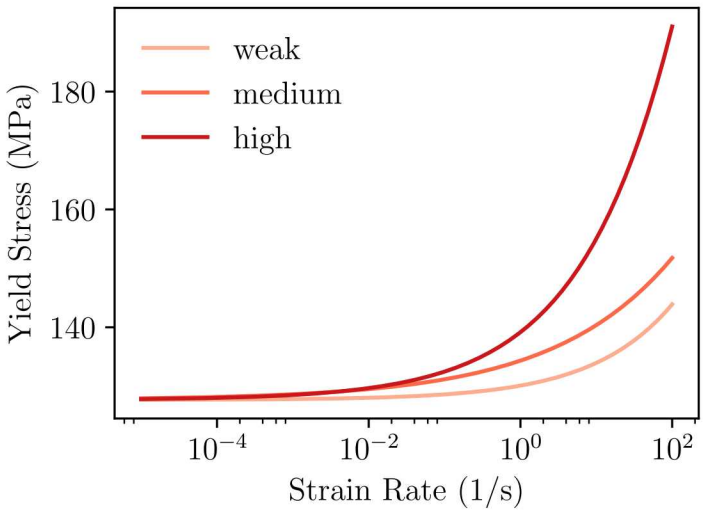

Figure 15: Rate dependence added to the material yield stress to add numerical stability to the pipe bomb simulations.

4.3 Adding Rate Dependence for Numerical Stability

After finishing the calibrations, we attempted to run the nominal pipe bomb simulations; however, the material model was having difficulty converging when the pipe bombs were about to fail. Since we knew the material model with rate dependence from the scoping simulations ran well, we added a small amount of rate dependence to the yield stress. This was done so that the added rate dependence had a negligible affect on the calibration results, but added enough numerical stability to the simulation that the material model and adagio could converge. Three levels of rate dependence were investigated and Figure 15 shows the effect that the rate dependence would have on the material yield stress. All pipe bomb simulations run to completion with the medium rate dependence from Figure 15. The medium rate dependence had values of $n = 37539$ and $f = 3.57$. The rate dependence was implemented using the flow stress rate dependence defined by Eq 3 in Section 2.2. At strain rates less than 1e-2 $\frac{1}{s}$, the added rate dependence changed the yield stress by approximately 1%. The nominal simulations show that once the pipe bomb reaches these strain rates they fail within less than a second because the pressure loaded structure has become unstable. As a result, the added rate dependence does not influence the failure pressure of the simulations.

4.4 Damage Model Calibration

Although the failure of the pipe bomb specimens is driven by a structural instability, damage was added to the material model to enable crack initiation and propagation through element death. We calibrated damage to the tests with a strain rate of 0.1 $\frac{1}{s}$ and a temperature of 973.15 K because these tension tests more closely matched the high-rate, high-temperature

Table 5: Calibrated damage parameters

Model Parameter	**Calibrated Value**
ϕ_0 (.)	1e-4
m (.)	3.5
max damage (.)	0.5

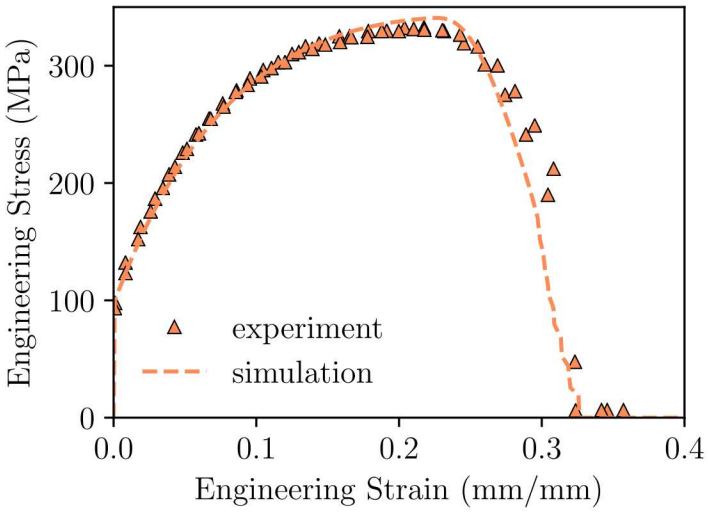

Figure 16: Results from the tension specimen simulation with calibrated local damage model plotted with the experimental data. The simulation and experiments were performed at a strain rate of 0.1 $\frac{1}{s}$ and a temperature of 973.15 K

conditions expected at failure for the pipe bomb specimens. The calibration was performed manually and the goal was to reduce the error between the simulation and experimental engineering stress-strain curves. Due to the use of a local damage model, the solution post bifurcation is mesh dependent.[5] In order to reduce the errors introduced by the mesh dependent local damage model, the same element size was used for both the tension specimen simulation for damage calibration and the pipe bomb model simulations. The final calibrated damage parameters are listed in Table 5 and Figure 16 shows the results of the calibration. Once a material point reaches maximum damage, the element is removed from the simulation using element death.

5 Nominal Simulations

Before proceeding to the uncertainty quantification study, a mesh convergence study was performed and simulations for each specimen were completed using the updated material model calibration. The mesh convergence study ensures that a converged mesh with minimal error is used for the uncertainty quantification study in the next section. We then compare the nominal simulations of each specimen to the experimental results to begin the validation process. Finally, we use the results from PB1 to verify our assumptions for the material model calibration.

5.1 Mesh Convergence

Using PB1, a mesh convergence study was completed using Richardson's extrapolation, which estimates an exact, or continuum (i.e. mesh size of zero), solution based on the results from three discrete solutions.[12] The three meshes were comprised of an initial mesh with three elements through the thickness of the pipe bomb wall and subsequently doubled to six and twelve elements through the thickness. Based on the results of these three discrete solutions (Table 6), Richardson's extrapolation estimates the continuum failure pressure to be 776.6 psi. The order of accuracy, p, for this estimate is 1.2, hence the near linear trend in Figure 17. A higher order of accuracy could be achieved by running an additional level of refinement (24 elements through the thickness), but this would result in a 56 million element model, which is not practical. The baseline mesh has a sufficiently low error (<1%) to conclude that the mesh does not significantly contribute to the failure pressure error. Therefore, the baseline mesh was chosen for the nominal simulations of each considered pipe bomb and the uncertainty quantification.

Table 6: Simulation results for three discrete meshes of the PB1 specimen.

Mesh	Elements Though Thickness	Element Size (in)	Number of Elements	Failure Pressure (psi)	Error
Coarse	3	0.0067	112,400	793.3	2.1%
Baseline	6	0.0033	883,952	783.9	0.9%
Fine	12	0.0017	7,003,744	779.8	0.4%

5.2 Results

Each pipe bomb specimen was simulated using the baseline mesh and the nominal material model parameters determined in Section 4.2. Tables 7 and 8 give the failure pressures and temperatures for each of the considered pipe bomb simulations as well as the corresponding experimental results, respectively. For all specimens, the failure pressure was over predicted using the nominal material model calibration. For PB9, the experiment fails at a much lower temperature than the other pipe bomb models. The experimental data shows that it

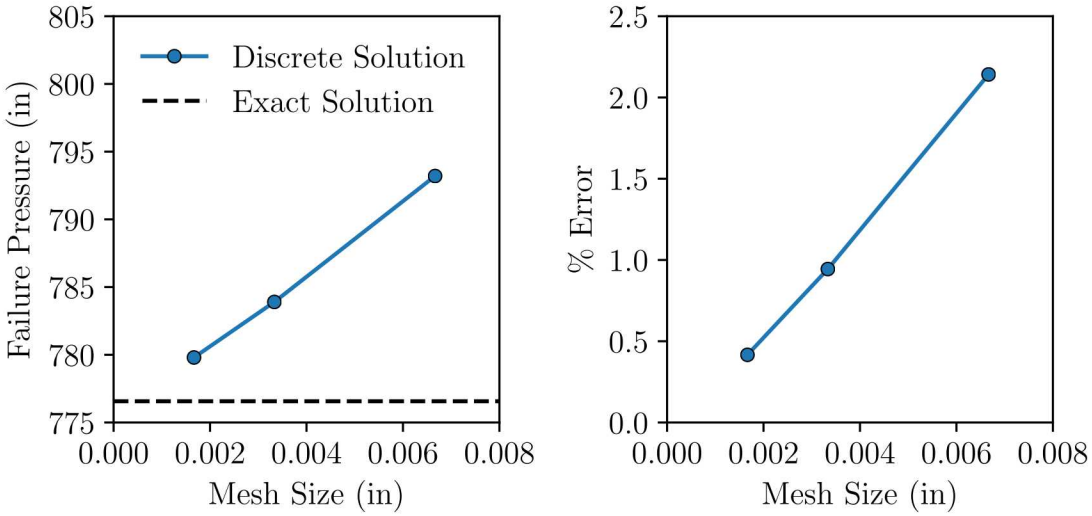

Figure 17: Mesh convergence study results.

failed at about 600 K, which is not a temperature where we calibrated the material model to be accurate at high strains. Pipe bomb simulation PB2 also has much higher errors than the other simulations even though it failed at a temperature where we believe the material model should be valid. We suspect this noticeably larger error may be due to errors in the temperature interpolation algorithm.

The failure path predicted by the simulation was correct. Figure 18 shows an image of the simulation during the catastrophic failure event. During the simulation, the time step reduces from 12 seconds to microseconds in order to temporally resolve the explosive failure. As with the experiments, the crack forms due to hoop stress and propagates axially along the specimen. Once the crack reaches the radius at the end of the gage section, it begins to propagate circumferentially on both ends. After the crack propagates to the end of the gage section, the solution is suspect because we would need to consider the fluid-structure interaction between the pipe bomb specimen and pressuring gas to include the correct pressure reduction rate.

5.3 Validating the Material Model Calibration Assumptions

After running the nominal simulations, we verified that the plastic strains, plastic strain rates and temperatures we focused on for calibrating the material model were valid. To do so, we created two-dimensional histograms of the element plastic strains, plastic strain rates, and temperatures for every time step for each specimen simulation. Figures 19, 20 and 21 show these histograms for pipe bomb model PB1. By looking at the histograms, it is clear that the elements below 873.15 K never experience more than 0.15 plastic strain and the majority of elements with plastic strains greater 0.4 are at rates above 1e-3 $\frac{1}{s}$. These results support the calibration decisions described in the beginning of Section 4.2. The remaining

Table 7: Nominal simulation failure pressures

	Failure Pressure (psi)		
Specimen	**Experiment**	**Simulation**	**Error**
1	605.5	783.9	+29.4%
2	587.0	833.6	+42.0%
4	655.2	792.1	+20.9%
8	637.5	752.5	+18.0%
9	732.0	1066.4	+45.7%
10	647.0	850.3	+31.4%
15	633.7	779.1	+22.9%
16	637.3	786.8	+23.5%

Table 8: Nominal simulation failure temperatures. Data marked with '*' lost thermocouples before failure.

	Failure Temperature (K)		
Specimen	**Experiment**	**Simulation**	**Error**
1	957.5	1003.6	4.8%
2	944.75	956.9	1.3%
4	984.25	1020.1	3.6%
8	924.0*	1068.4	15.6%
9	559.75	701.4	25.3%
10	926.75*	951.1	2.6%
15	863.45*	1039.4	20.4%
16	897.5*	1046.9	16.6%

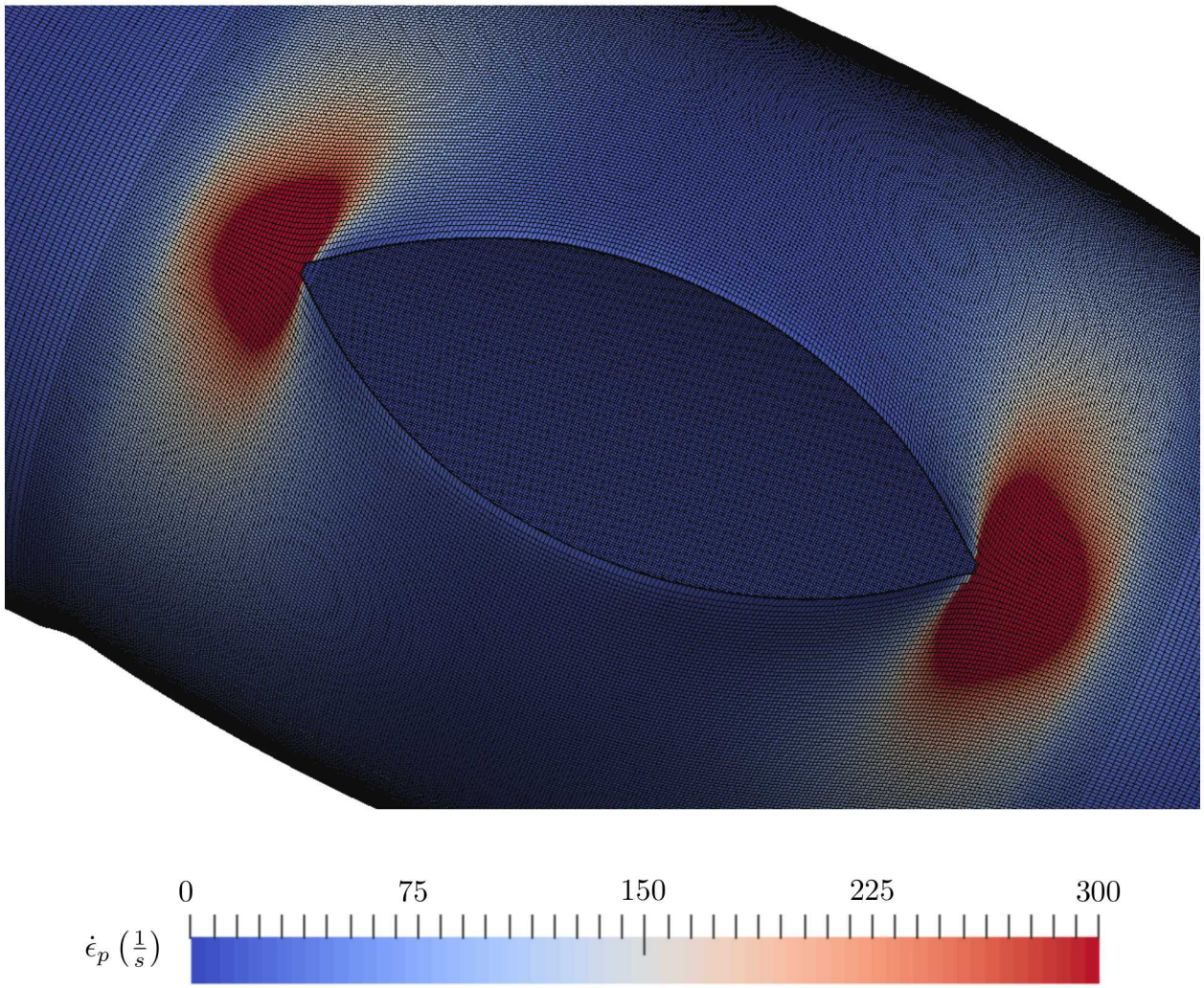

Figure 18: Failure image of PB10 showing the axial crack path along the specimen. Once the crack reaches the thicker material at the end of the gage section it propagates circumferentially in both directions at both ends.

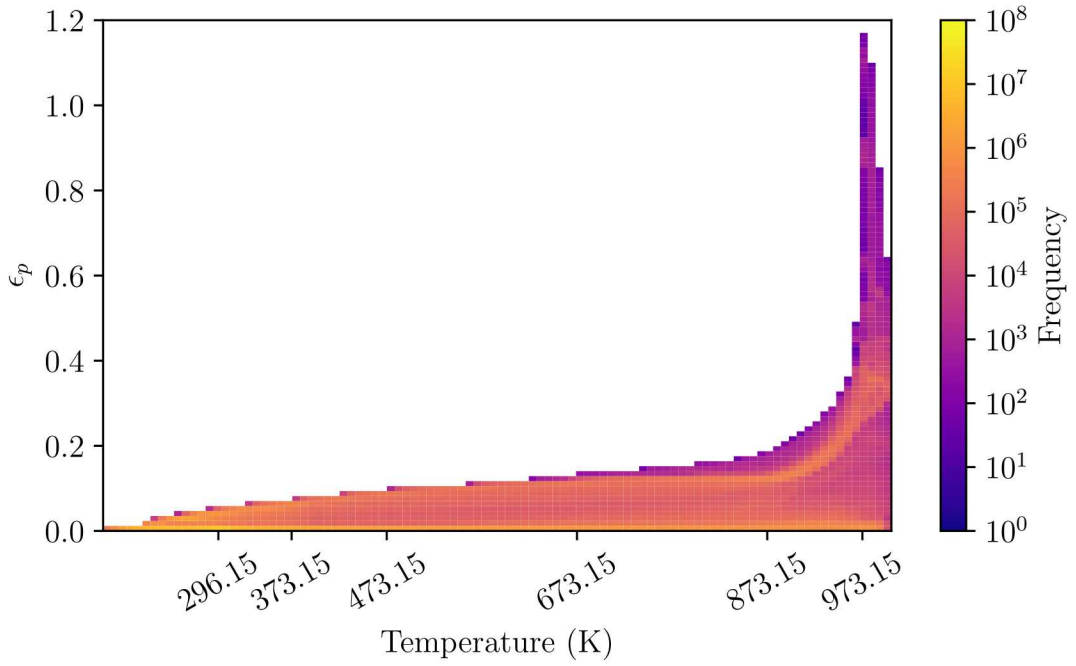

Figure 19: Histogram of element plastic strain and temperature for all simulation time steps.

histograms for all other nominal pipe bomb simulations are in Appendix B.

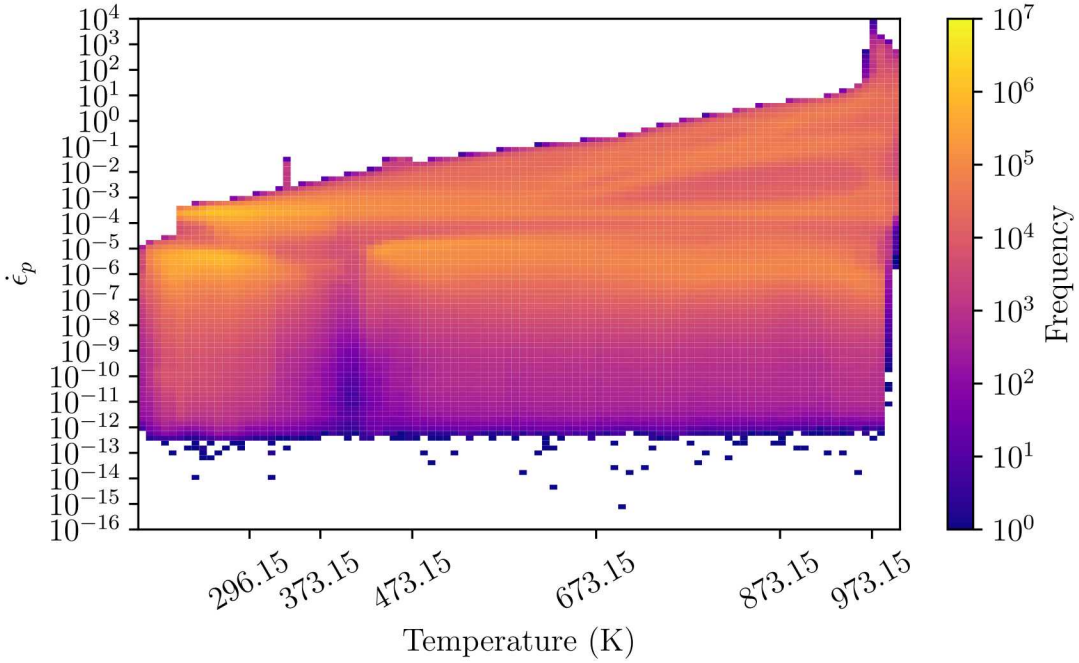

Figure 20: Histogram of element plastic strain rate and temperature for all simulation time steps.

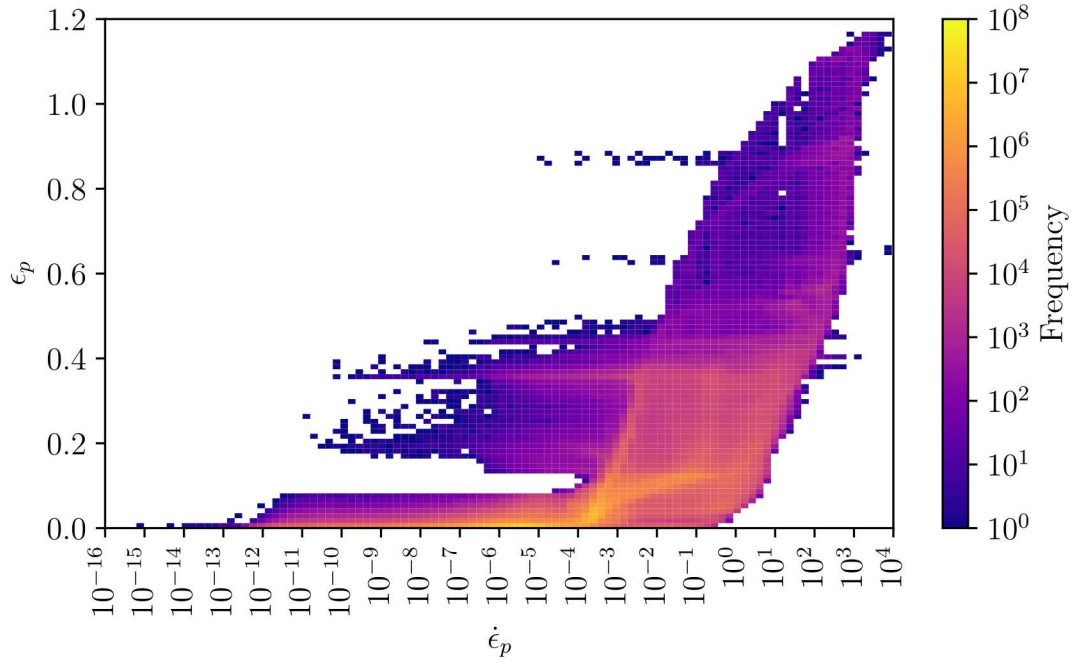

Figure 21: Histogram of element plastic strain and plastic strain rate for all simulation time steps.

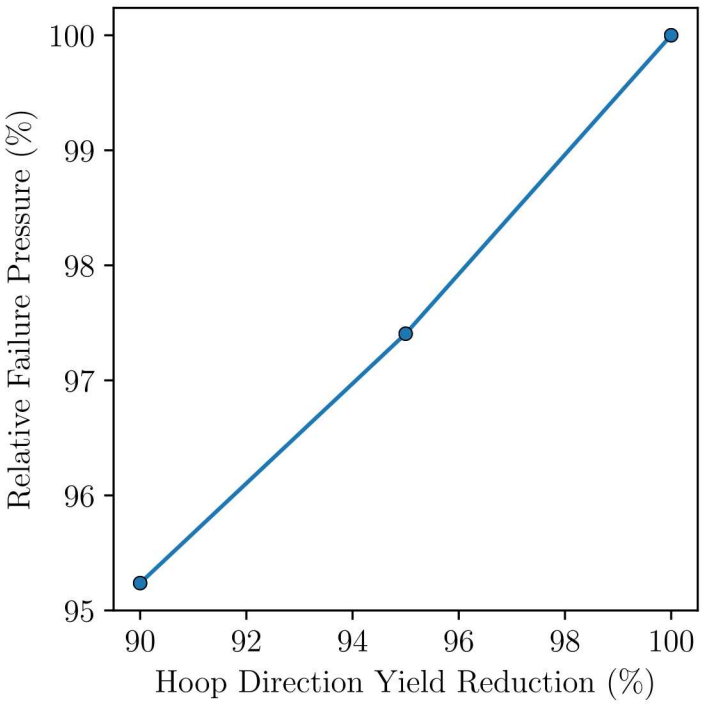

Figure 22: Failure pressure of the PB1 model as the hoop direction yield is reduced. The failure pressures are relative to the failure pressure of the simulation with the HPD material model and isotropic yield. This simulation failed at 895.7 psi.

6 Qualitative Assessment of Anisotropic Yield on PB1's Failure Pressure

As mentioned in the introduction, the effect of anisotropic yield was investigated for the pipe bomb models. Since the pipe bomb is manufactured from extruded tube, the microstructure texture and elongated grains that arise from this manufacturing process can cause anisotropic inelastic behavior. To simulate the pipe bomb with anisotropy, we used the Hill Plasticity Damage (HPD) material model in SierraSM. This model includes BCJ rate dependence on the flow rule, BCJ like Voce hardening, the Hill 48 yield surface [8] and the damage model from BCJ. One important difference is that HPD does not have static recovery. As a result, only a qualitative assessment is made here which can be used to estimate an approximate percent reduction in failure pressure due to anisotropy. To populate the HPD material model, only a few changes were made to the calibrated parameter set from Section 4.2. The primary change was that the yield was reduced in the hoop direction. The decision to reduce the yield in the hoop direction was based on our experience with rolled sheet which generally has a higher yield in the rolling direction. The only other change was to set the dynamic recovery term to the average of R_d^{873} and R_d^{973}. This was done because HPD does not currently have temperature dependent dynamic recovery. The calibrated HPD material

model file is included in Appendex C.2.

The pipe bomb model PB1 was used for this assessment and was ran with an isotropic form of HPD, HPD with 5% lower yield in the hoop direction and HPD with 10% lower yield in the hoop direction. Figure 22 shows how the failure pressure decreases with a decrease in the hoop direction yield stress. From these results, we can expect a failure pressure reduction of approximately one half of the percentage reduction of the hoop direction yield stress. Since the 10% drop in yield stress for the hoop direction yield is most likely a high upper bound, these results show that anisotropy is not a likely cause of the high errors for the failure pressures predicted by the simulations.

7 Uncertainty Quantification

Continuing the validation process the pipe bomb simulations, an uncertainty quantification study is used to account for the stochastic nature of the various inputs used in the simulation. While there are several sources of uncertainty for the pipe bomb, only the variability of the material and geometry were considered when determining the uncertainty of failure pressures. The uncertainty quantification study will first account for the material variability before incorporating the geometric variability in order to provide insight into the relative impact of the two sources of uncertainty. Unlike the nominal simulations, only PB1 was considered in the uncertainty quantification study, which corresponds with what was done in the previous work.

7.1 Material Uncertainty

While the uncertainty in some material properties can be experimentally determined, the equations for the temperature dependent stress-strain response that governs the failure of the pipe bomb requires calibration. In Section 4.2, twelve parameters were calibrated to give the constitutive equations of the material model a similar response to the experimental data. For uncertainty quantification only eleven parameters were used and Y_5 was held constant. In order to generate statistical distributions for each of the material model parameters, hundreds of additional calibrations were computed using bootstrapping sampling of the existing experimental data. The parameter distributions were then sampled to propagate the material uncertainty through the PB1 simulation to provide a possible range of failure pressures.

Bootstrapping

Often it is not possible to examine an entire population, so a sample that is only a fraction of the population is examined. From that sample, the mean and variance of the population can be inferred and in order to determine the variance of the mean, additional samples would be required. Bootstrapping is a statistical method that samples the available data with replacement (re-sampling) to provide an estimate of the variance of the original sample set mean when additional samples of the population are not feasible.[7] Given a sample set of size N, bootstrapping will re-sample that sample set to create a re-sample of size N, as shown in Figure 23. This process is repeated many times such that a distribution for the mean can be computed.

The experiments done to characterize the 304L stainless steel provide samples of the stress-strain curves for six temperatures: 296.16 K, 373.15 K, 473.15 K, 673.15 K 873.15 K, and 973.15 K. All temperatures were tested at a rate of 0.001 $\frac{1}{s}$ with additional experiments done at 973.15 K for rates of 0.01 and 0.1 $\frac{1}{s}$. As described in Section 4, MatCal implicitly calibrates the average stress-strain response by minimizing the error from all curves at

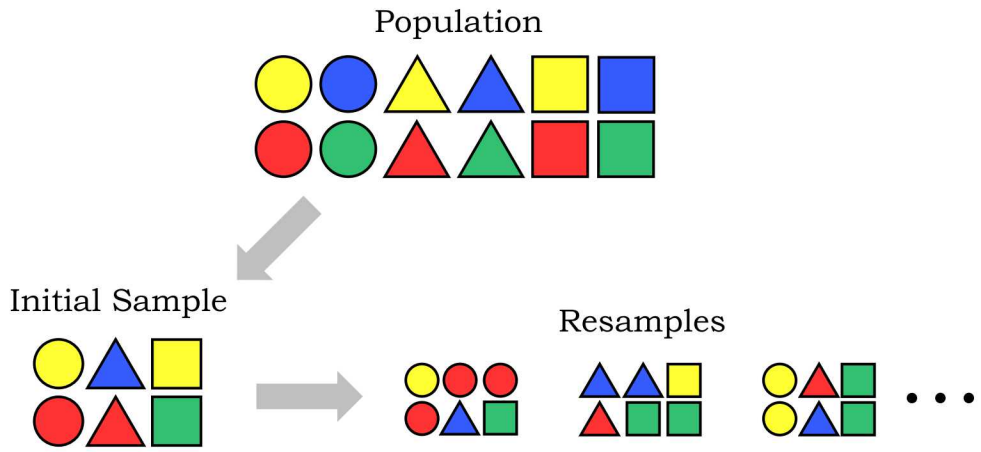

Figure 23: Example of bootstrapping.

each temperature/rate combination, which results a single 'average' set of material model parameters. Bootstrapping was employed to generate re-samples of the experimental data at each temperature/rate combination to provide an estimate of the variance for each material model parameter. Table 9 shows examples of the re-sampling of the experimental data sets for each temperature/rate combination. While the experimental data sets for a particular temperature and rate may repeat between re-samples, each re-sample remains unique when considering all temperatures and rates.

Table 9: Examples of bootstrapping re-samples.

Temperature	**Rate**	**Initial Sample**	**Re-sample 1**	**Re-sample 2**	**Re-sample 3**
23°C	0.001 in/s	[0, 1, 2, 3, 4, 5]	[1, 1, 2, 2, 4, 5]	[1, 2, 3, 3, 5, 5]	[2, 2, 3, 5, 5, 5]
100°C	0.001 in/s	[0, 1, 2, 3, 4]	[0, 3, 3, 4, 4]	[0, 1, 2, 3, 4]	[0, 1, 2, 2, 2]
200°C	0.001 in/s	[0, 1, 2, 3, 4]	[0, 3, 3, 4, 4]	[1, 1, 1, 2, 3]	[0, 0, 0, 2, 4]
400°C	0.001 in/s	[0, 1, 2, 3, 4]	[0, 2, 3, 3, 4]	[0, 0, 1, 2, 3]	[1, 2, 2, 3 ,3]
600°C	0.001 in/s	[0, 1, 2]	[0, 0, 1]	[0, 1, 2]	[0, 1, 1]
700°C	0.001 in/s	[0, 1, 2, 3, 4, 5]	[1, 1, 3, 3, 4, 5]	[1, 4, 4, 4, 5, 5]	[1, 2, 3, 4, 4 , 5]
700°C	0.01 in/s	[0, 1]	[0, 1]	[0, 1]	[1, 1]
700°C	0.1 in/s	[0, 1]	[0, 0]	[1, 1]	[0, 1]

Parameter Uncertainty

Using the sets of bootstrap re-sampled experimental data, additional calibrations were run with MatCal. The hybrid approach, that was used for the material calibration described in Section 4.2 was considered too computationally expensive for the number of calibrations needed to generate statistical distributions for the material model parameters. Since the re-samples do not introduce drastic changes to the composition of the experimental data

sets, the material model parameters from subsequent calibrations will not vary significantly. Therefore, it was assumed that the re-sampled material model parameters would globally reside near the model parameters found by the hybrid approach in Section 4.2. Using a local, non-gradient based algorithm with a reduced parameter space would be ideal to calibrate the re-sampled experimental data sets. Specifically, the mesh adaptive search algorithm was employed with parameter bounds set at $\pm 15\%$ from the initial point set by the material model parameters in Section 4.2. The mesh adaptive search generates a denser search pattern that migrates towards the converged solution each iteration. A total of 517 additional calibrations were performed. Of these, thirty-five were removed: twenty-three calibrations failed to provide parameters that differed from the initial point and twelve calibrations provided a bounding value for R_s (upper bound eleven times and the lower bound once). The removal of these calibrations eliminates calibrations with incorrect values while not significantly affecting the shape of the parameter distribution, as shown in Figure 24.

For each of the eleven material model parameters, fits for several statistical distributions available in Dakota (uniform, normal, gamma, Gumbel, and Weibull) were performed using Python's SciPy library. Python returned the Maximum Likelihood Estimate (MLE) for the parameters defining each distribution, which was computed by maximizing a log-likelihood function using a penalty factor for samples outside the range of the distribution.[9] However, this method is not guaranteed to return the optimal global solution for a particular parameter. In order to quantitatively assess how well each fit matches the re-sampled data, quantile-quantile plots (Q-Q plots) were used. The Q-Q plot compare the observed quantiles against the quantiles determined from the fitted distribution - if the fit is an exact match, the plotted quantiles will fall on the line $y = x$. To assess which fit most closely matches the data, the coefficient of determination, or R^2, was calculated to provide a value of how well the Q-Q plot matched the line $y = x$. R^2 is given by:

$$R^2 = 1 - \frac{SS_{res}}{SS_{tot}} = 1 - \frac{\sum_i (y_i - x_i)^2}{\sum_i (y_i - \bar{y})^2} \tag{4}$$

where y_i is the observed quantile value, x_i is the theoretical quantile value from the fit, and $\bar{y}$ is the average observed value. Figure 25 shows an example of Q-Q plots and demonstrates how the Q-Q plots were used to assess normal and uniform distribution fits to the parameter Y_1. In general the fit with the maximum R^2 value was considered to be the best fit; however, if no fit was significantly better than a normal distribution, the normal distribution was chosen for simplicity. Table 10 provides a summary of the best distributions and their parameters, and histograms and Q-Q plots of selected distributions for all parameters are provided in Appendix A.

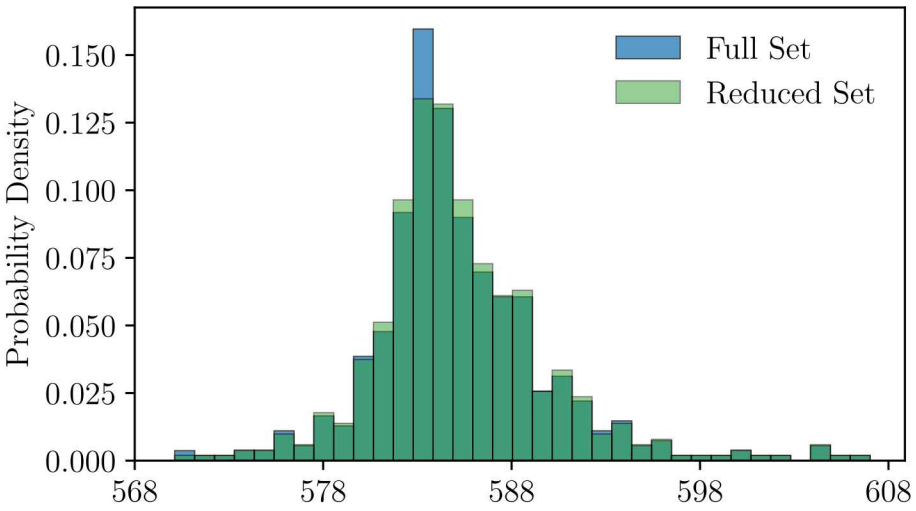

(a) Y_0

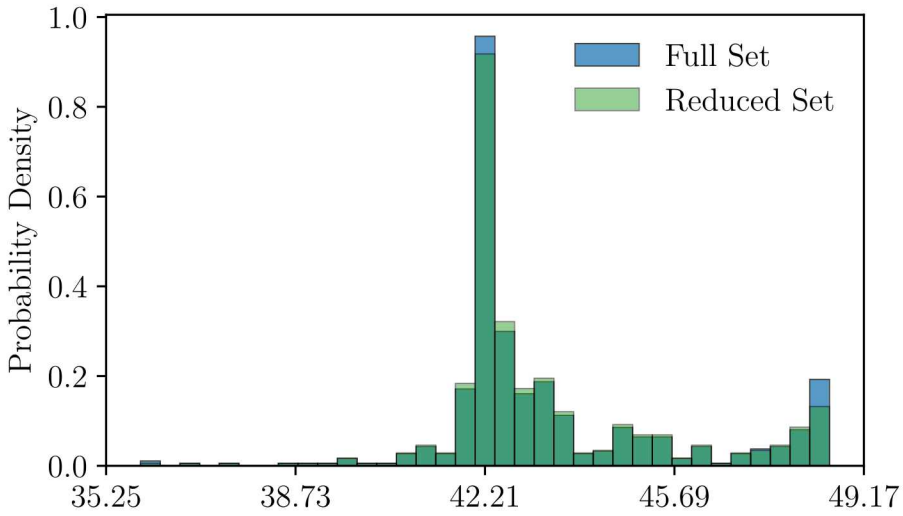

(b) R_s

Figure 24: The full set of calibrations compared to the reduced set.

Using bootstrapping re-samples to generate statistical distributions for material model parameters provides several insights:

- While the fitted distributions capture the general tend, they were unable to capture the spike in observed results near the initial point. This is due to the fact that for a given calibration, all eleven parameters did not change significantly from the their initial points (eliminating calibrations with parameters within a small tolerance of the initial point would result in very few calibrations). This introduces a bais that is a result of using a local optimization method starting near the optimal solution rather than a global optimization method when calibrating the re-samples.
- Well defined distributions are not guaranteed. For example, R_s shows what looks to be a bi-modal distribution in Figure 24 and was slightly affected by undersized bounds. In this case, a normal distribution was assumed, which will capture the increase in probability near the mean, but not at the right tail.

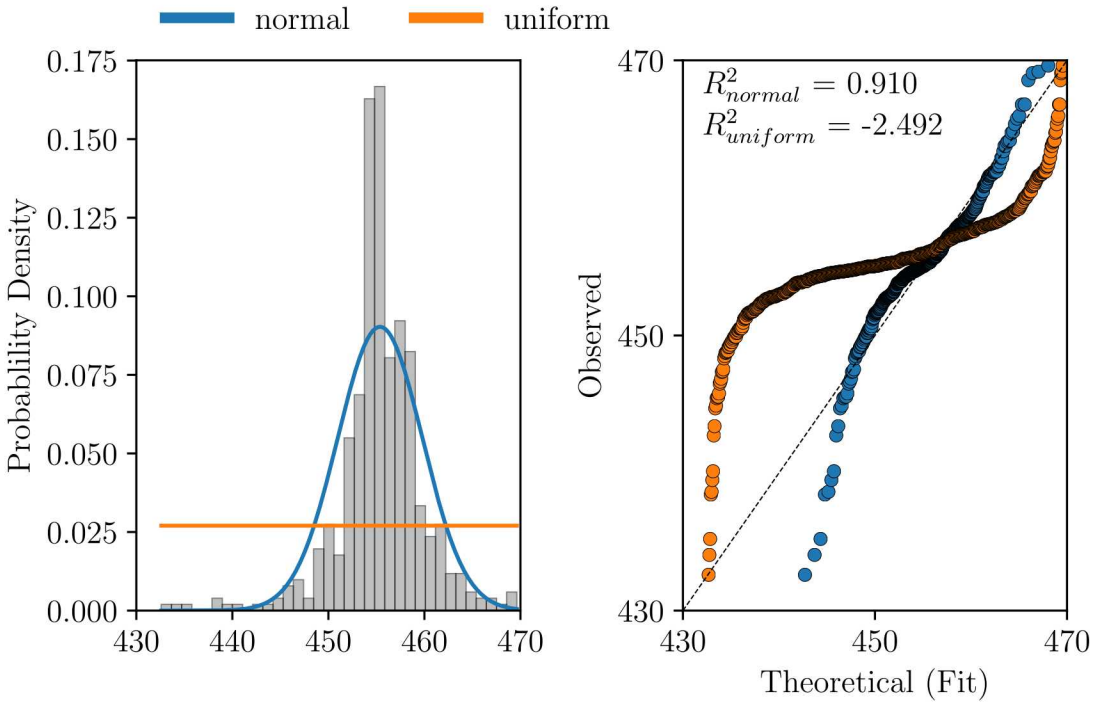

Figure 25: Q-Q plot comparison between uniform and normal distributions fits for the parameter Y_1.

Table 10: Material model parameter distributions.

Model Parameter	**Distribution**	**Distribution Parameters**
Y_0	gamma	$\alpha = 27.32, \beta = 0.89, initial\_point = 560.95$
Y_1	normal	$\mu = 455.38, \sigma = 4.42$
H	gamma	$\alpha = 53.70, \beta = 2.23, initial\_point = 3413.8$
R_d^{296}	normal	$\mu = 3.77, \sigma = 0.06$
R_d^{373}	normal	$\mu = 5.41, \sigma = 0.09$
R_d^{473}	normal	$\mu = 5.87, \sigma = 0.09$
R_d^{676}	Weibull	$\alpha = 10.86, \beta = 0.77, initial\_point = 6.25$
R_d^{873}	Gumbel	$\alpha = 11.26, \beta = 7.79$
R_d^{973}	normal	$\mu = 9.09, \sigma = 0.05$
Q_s	gamma	$\alpha = 52.47, \beta = 0.007, initial\_point = -12.77$
R_s	normal	$\mu = 43.35, \sigma = 2.09$

Results

In order to propagate the uncertainty in the material model parameters and determine their influence on the failure pressure of the pipe bomb model, the parameters' distributions were sampled using Dakota and included in the pipe bomb simulation's material file. The samples of the distributions were taken using Latin Hypercube sampling (LHS), which is a stratified sampling approach that creates a set of equi-probable bins in the n-dimensional parameter space.[1] In order to ensure adequate coverage of the parameter space, the number of bins created for each parameter should be at least $n + 1$. LHS requires fewer samples than a purely random sampling approach to provide converged statistics, with the mean generally converging quickly and the standard deviation requiring additional sampling. Therefore, to ensure convergence for the failure pressure statistics of the pipe bomb simulation, several sample sets were analyzed. Furthermore, a Gaussian Process (GP) surrogate was built from each sample set to verify the convergence of the standard deviation and to calculate the Sobol Indices. Sobol Indices quantify the influence of each parameter on the quantity of interest.[1]

The wall thickness of the pipe bomb, which will be examined in the subsequent section, was included as a constant variable with a value of 0.020 inches (same as the nominal simulation) for this study in order to determine the failure pressure solely based on the variability of the material model parameters. To maintain sample size consistency between this study and the following section, the initial sample set was set to $n + 2$, or 13, samples and subsequent samples were systematically double to a size of $16(n + 2)$, or 416, samples. Table 11 shows the development of the mean and standard deviation with respect to the sample size for both the LHS and GP models. Even though the sampling and surrogate studies give similar results, when plotting each study (Figure 26), a better representation of the failure pressure distributions is given by the surrogate model due to the greater number of samples (140,000 compared to 52 or 104). This shows that the distribution is slightly skewed to the left, which is hard to distinguish in the LHS study. Due to this skew, a Weibull distribution may be more appropriate to represent the failure pressure based on the uncertainty in the material

Table 11: Surrogate model mean failure pressure and standard deviation.

Samples	**LHS Mean (psi)**	**LHS Std. (psi)**	**GP Mean (psi)**	**GP Std. (psi)**
13	789.2	5.60	789.0	5.75
26	788.9	6.43	789.0	6.32
52	788.5	6.59	789.0	6.86
104	788.5	6.55	788.8	6.67
208	788.6	6.68	788.7	6.63
416	788.7	6.66	788.7	6.64

Now that the uncertainty of the failure pressure of the pipe bombs has been determined, by using the surrogate model results the Sobol Indices can be calculated to quantify the influence of each parameter on the PB1 simulation's failure pressure. For each parameter, a main index and a total index will be calculated. The main index represents the portion

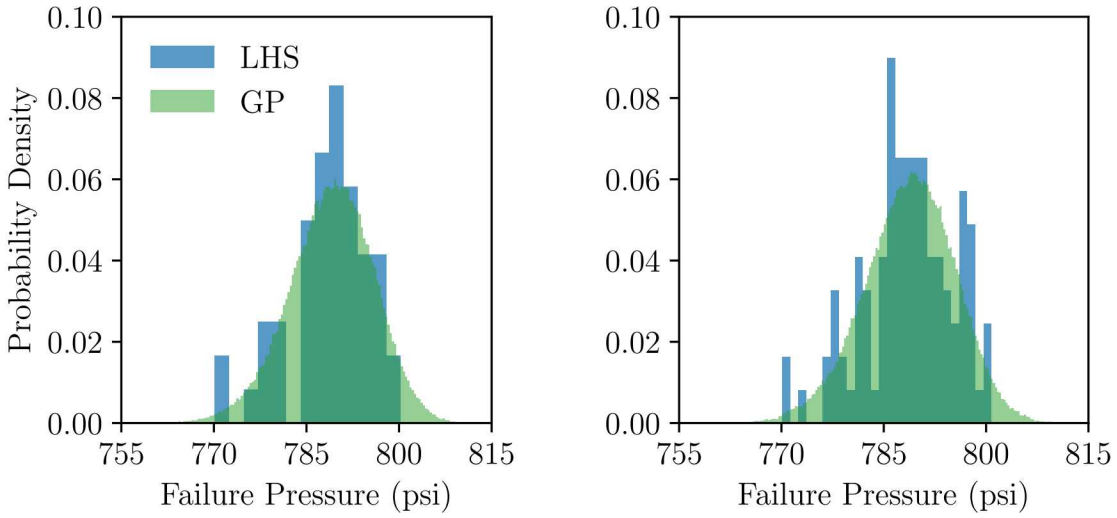

(a) 52 samples

(b) 104 samples

Figure 26: Comparison of LHS and GP distributions.

of the variability of the failure pressure that can be attributed to a particular parameter independent of the other parameters, where as the total index represents the portion of the variability for each parameter including any correlations with other parameters. Table 12 shows the main Sobol Indices calculated from each sample size, showing that convergence was reached at 208 samples. The total Sobol Indices were not shown as the correlation between parameters did not affect the level of significance for the parameters. Of the eleven parameters used to describe the material model, only six (Q_s, H, R_s, R_d^{973}, Y_0, and $Y1$) show any appreciable influence on the failure pressure.

Table 12: Main Sobol Index by sample size

Samples	**13**	**26**	**52**	**104**	**208**	**416**
Q_s	49.2%	55.9%	53.9%	58.1%	59.0%	59.9%
H	21.4%	13.6%	11.6%	11.8%	12.4%	12.1%
R_s	14.9%	10.8%	10.2%	10.0%	10.8%	10.6%
R_d^{973}	7.3%	6.5%	8.3%	7.5%	7.8%	7.7%
Y_0	5.8%	8.1%	5.9%	7.4%	6.4%	6.3%
Y_1	0.2%	2.3%	2.0%	1.7%	2.0%	1.8%
R_d^{296}	0.0%	0.0%	1.5%	0.6%	0.2%	0.0%
R_d^{373}	0.2%	0.1%	0.4%	0.1%	0.1%	0.0%
R_d^{473}	0.0%	0.2%	0.6%	0.4%	0.1%	0.0%
R_d^{673}	0.1%	0.0%	0.3%	0.0%	0.0%	0.0%
R_d^{873}	0.0%	0.3%	1.3%	0.1%	0.0%	0.1%

7.2 Geometry Uncertainty

In addition to the material uncertainty the failure pressure of the pipe bomb is also influenced by variations in geometry as each pipe bomb was not manufactured perfectly to nominal specifications. The wall thickness of the reduced region in the pipe bomb was the only dimension where the specified tolerances had any significance (Figure 6) and was the only dimension investigated.

Wall Thickness

The nominal inner diameter of the extruded tube used for the pipe bomb was specified as 3.00 inches with an unspecified tolerance and the outer diameter of the reduced region was machined to 3.040 $\pm$ 0.001 inches. This gives a nominal thickness of 0.020 inches in the failure region with an unknown tolerance. In order to determine the true wall thickness in the reduced region, the specimens were measured by resting inner diameter of the pipe bomb on a cylindrical shaft and measuring the outer diameter with a fixed dial indicator, as shown in Figure 27. The thicknesses for all considered pipe bombs are summarized in Table 13. It should be noted that it is unclear how many locations along the axis of the pipe bomb were measured in order to determine the minimum and maximum wall thicknesses.

With the exception of PB4, the wall thickness falls between 0.018 and 0.022 inches. However, the measurement method is fundamentally flawed. As shown in Figure 27, the measurement shaft will contact the pipe bomb at two 'high' spots of the inner diameter. For instance, if measurements were taken at points A and C in Figure 27, the true thickness would be captured, but if taken at point B, the thickness would be over predicted. This is then exacerbated by the fact that the inner diameter was not machined and maintained its initially extruded surface. Since the wall thickness will never capture the actual minimum thickness and will not under predict any thickness, the validity of the measured minimum wall thicknesses is questionable. Therefore, the observed range of wall thickness was adjusted to be between 0.017 and 0.022 inches.

Since only the minimum and maximum values of the wall thickness were recorded, there is no indication of what distribution the wall thickness follows. Therefore, when including the geometric uncertainty with the material uncertainty, a uniform distribution was assumed.

7.3 Surface Roughness

As mentioned in previous section, the inner diameter was not machined but had a rough and visibly pitted surface a result of the extrusion process. Due to the roughness, stress concentrations will develop that can lower the failure pressure of the specimen. While it was not possible to replicate the inner diameter of the pipe bomb specimens of concern, as they were destroyed in testing, a small portion was analyzed using image topography to provide an estimate of the roughness as well as the size and shape of a notch. Figure **??** shows the

Table 13: Minimum and maximum measured wall thicknesses.

Specimen	**Minimum (in)**	**Maximum (in)**
1	0.019	0.022
2	0.020	0.022
4	0.020	0.024
5	0.020	0.022
7	0.019	0.022
8	0.020	0.021
9	0.019	0.0225
10	0.019	0.021
11	0.020	0.023
12	0.018	0.0215
13	0.019	0.022
14	0.019	0.022
15	0.019	0.021
16	0.020	0.021

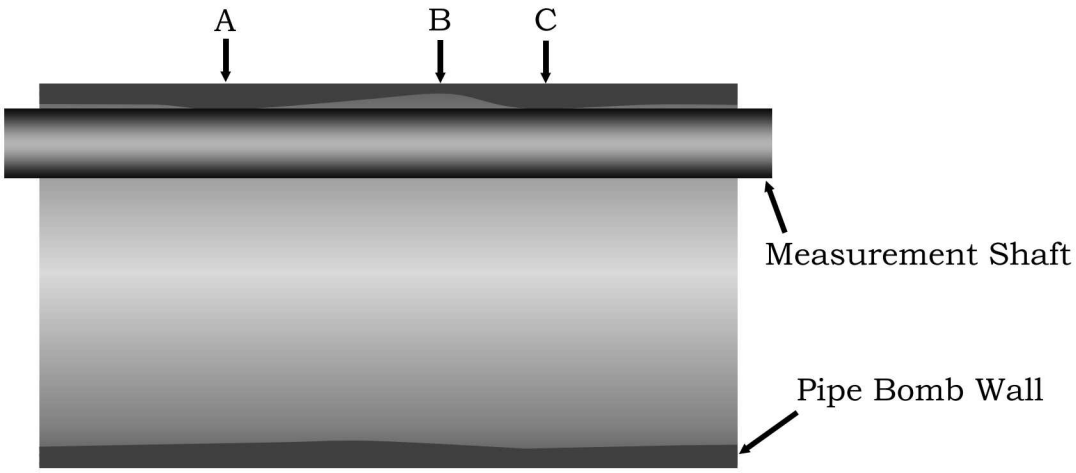

Figure 27: Wall thickness measurement diagram.

results of the image topography, which show the high and low points vary by as much as 0.0025 inches. In the figure a notch can be identified having a size of approximately 0.06 inches long by 0.01 inches wide and the depth is between 0.001 an 0.002 inches. Based on this data, notches on the inner diameter surface cut into a significant portion of the wall thickness by having depths ranging 5 to 10% of the wall thickness. As seen in Figure 29, a single notch oriented with the short axis along the axis of the tube and given a depth of 0.0015 inches was meshed for the pipe bomb geometry. The simulated failure pressure for PB1 was reduced by approximately 2% by including the notch. This demonstrates that the surface roughness contributes to the bias; however, it is hard to quantify without modeling the roughness on a more representative and larger region. Therefore, the surface roughness was not carried forward in the determination of the uncertainty of the failure pressure based on geometry uncertainty.

Results

Following the same process used for the material uncertainty, the uniform distribution for the wall thickness was included into the LHS and GP studies. Beginning at $n+1$, or 13, samples the sample size was systematically doubled until convergence was reached at $4(n+1)$, or 104, samples (Table 14). While convergence was checked based on the mean and standard deviation, when plotting the distributions of the LHS and GP studies in Figure 30, it is apparent that a normal distribution is not sufficient and a uniform distribution would be more appropriate. The Sobol Indices in Table 15 confirm that the wall thickness is much more influential than any of the material model parameters, hence the uniform appearance of the simulated failure pressures.

Table 14: Surrogate model mean failure pressure and standard deviation.

Samples	**LHS Mean (psi)**	**LHS Std. (psi)**	**GP Mean (psi)**	**GP Std. (psi)**
13	770.0	51.3	770.2	51.4
26	769.6	52.3	770.5	52.4
52	769.6	52.6	770.2	53.4
104	769.6	52.6	770.1	52.8

In order to quantify the relationship between wall thickness and the failure pressure, two additional studies were conducted with the wall thickness set to be constant at the minimum and maximum, receptively. A sample size of 104 was chosen based on the results of the previous studies and the mean failure pressures at each thickness were compared (Table **??**). The difference between the minimum and nominal thicknesses gives an average decrease in failure pressure of 36.9 psi per 0.001 inches, where as the difference between the nominal and maximum gives an average increase of 35.4 psi per 0.001 inches. Furthermore, the standard deviation increases as the wall thickness increases, indicating that as the wall thickens, the material variability has a greater affect on the failure pressure.

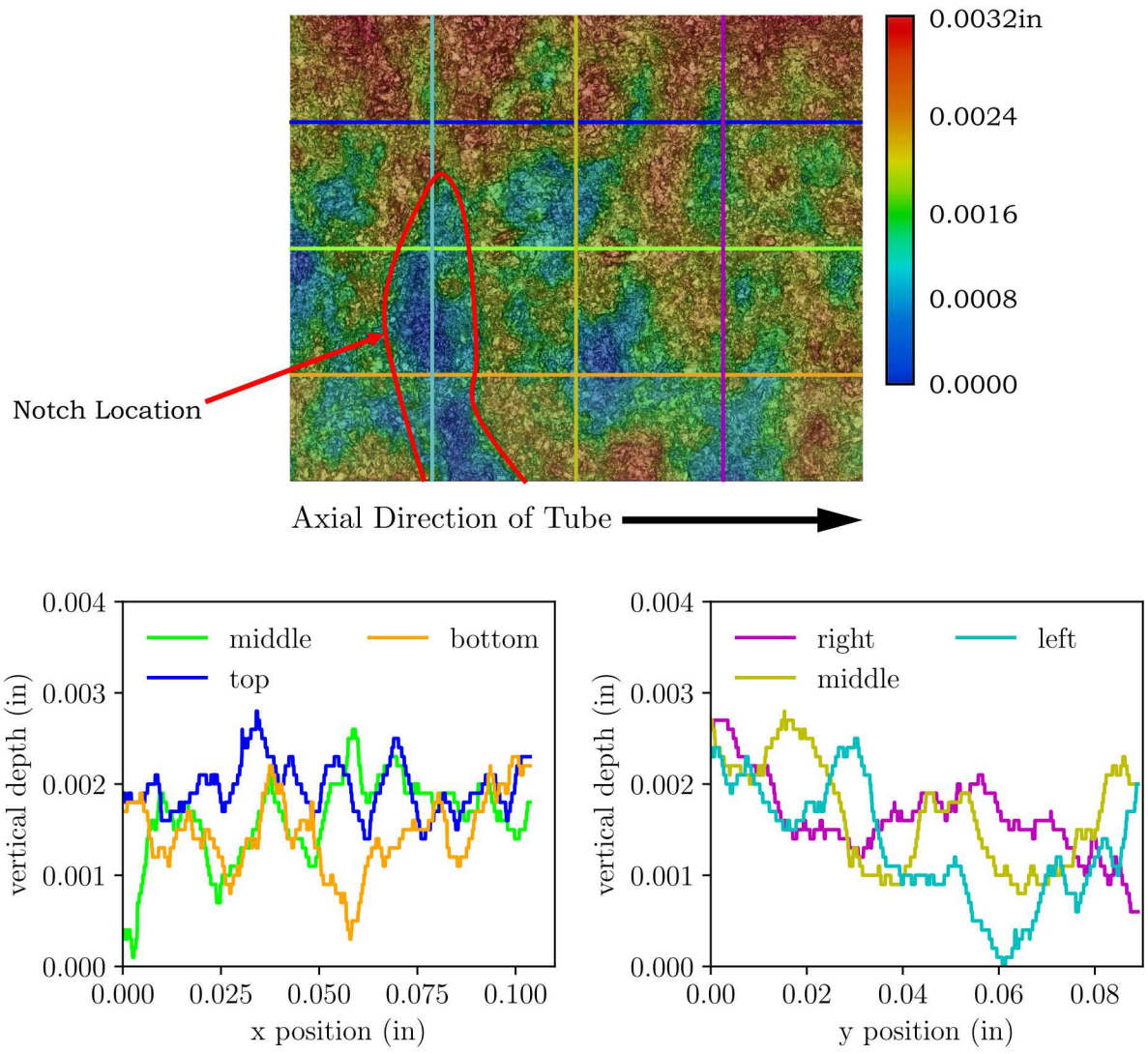

Figure 28: Image topography of the pipe bomb inner diameter.

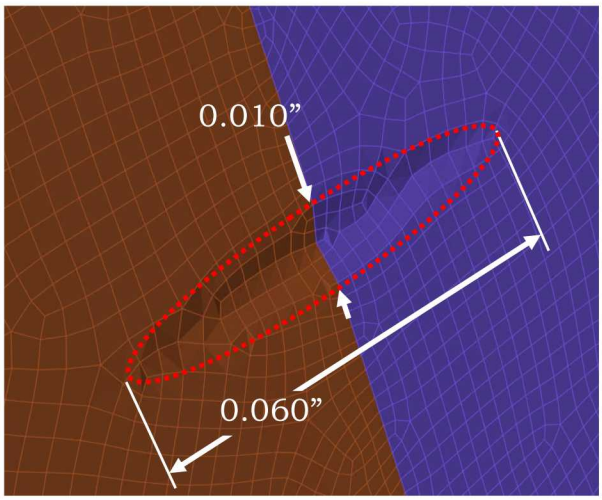

Figure 29: Shape and size of the meshed notch.

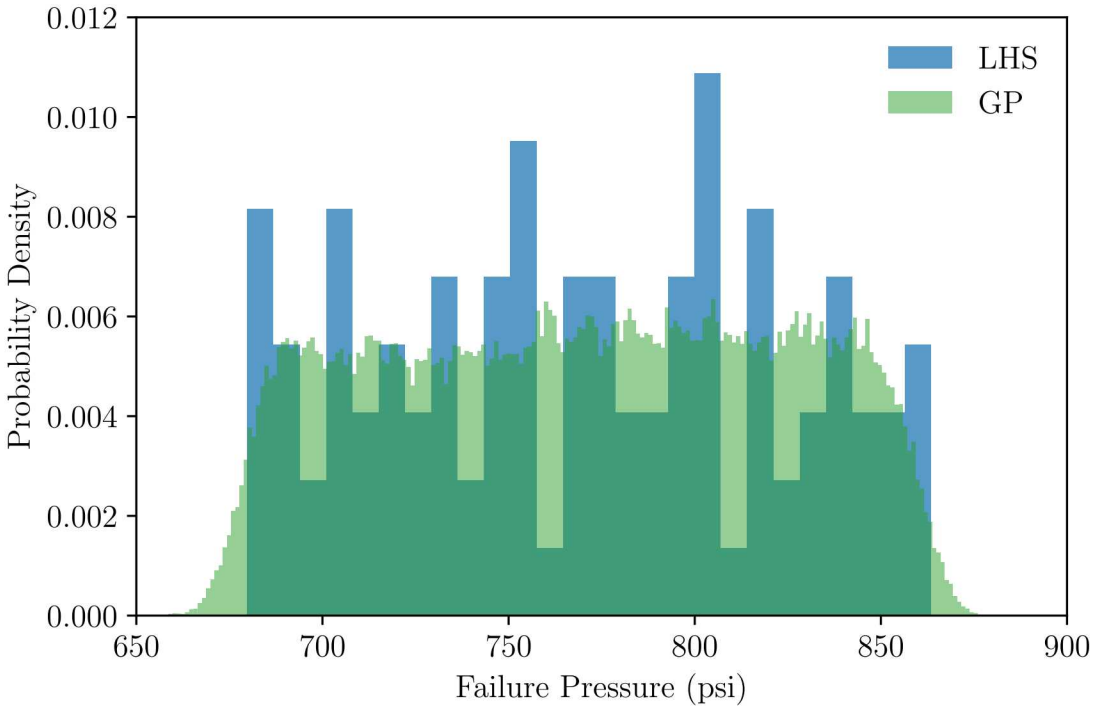

Figure 30: Failure pressure distribution with material and geometry uncertainty.

Table 15: Main Sobol Index by sample size

Samples	**13**	**26**	**52**	**104**
th_{wall}	98.0%	98.0%	97.9%	97.9%
Q_s	0.8%	0.9%	0.8%	0.9%
H	0.0%	0.1%	0.1%	0.1%
R_s	0.1%	0.1%	0.1%	0.1%
R_d^{973}	0.1%	0.1%	0.1%	0.1%
Y_0	0.1%	0.1%	0.1%	0.1%
Y_1	0.0%	0.1%	0.0%	0.0%
R_d^{296}	0.1%	0.0%	0.0%	0.0%
R_d^{373}	0.0%	0.1%	0.0%	0.0%
R_d^{473}	0.0%	0.0%	0.0%	0.0%
R_d^{673}	0.0%	0.0%	0.0%	0.0%
R_d^{873}	0.0%	0.0%	0.0%	0.0%

Table 16: Comparison of mean failure pressure for multiple wall thicknesses.

$\boldsymbol{th_{wall}}$ **(in)**	**GP Mean (psi)**	**GP Std. (psi)**
0.017	677.9	5.6
0.020	788.7	6.6
0.022	859.4	7.7

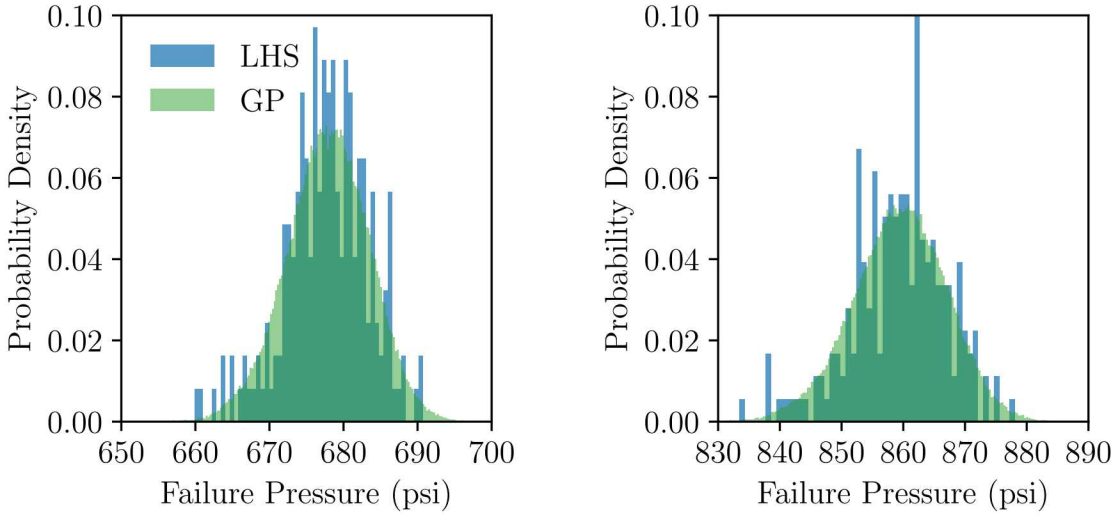

(a) $th_{wall} = 0.017$

(b) $th_{wall} = 0.022$

Figure 31: Distributions as various wall thicknesses.

8 Conclusion

As with the previous work by Romero, et. al. [14, 13], our simulations of the pipe bomb experiments using the BCJ material model over predicted the failure pressures. Also, when accounting for the variability associated with the material model, the resulting distribution of failure pressures did not encompass the experimental data. This lead to the incorporation of geometric variability, which showed a much higher impact on the simulation failure pressure variability. However, a lack of complete data regarding the wall thickness prevents any conclusion with respect to the final distribution of failure pressures. While success cannot be claimed for the simulated failure pressures, several important conclusions were drawn:

- Incorporating geometric variability into the uncertainty quantification showed that the wall thickness had a far greater influence on the failure pressure than any other variable and accounted for 98% of the variability seen in the failure pressure. A change in the wall thickness of 0.001 inches (5%) produced a 35-37 psi change in the failure pressure and the measured range of wall thicknesses spans 0.006 inches. Therefore, accurately controlling and measuring the wall thickness would be a necessary step towards accurately predicting the failure pressure.

- The temperature mapping algorithm may be a larger source of error than assessed by the previous pipe bomb modeling effort.[14, 13] The validation of the temperature algorithm was performed against a fully-coupled, thermo-mechanical simulation thought to be representative of PB1 and PB2. A potential short coming was that this simulation neglected convection. In the pipe bomb test environment, convection could potentially change the general shape of the temperature field on the specimen. The interpolation algorithm may account for this within the thermocouples; however, it cannot be trusted to extrapolate outside of the thermocouple region. Results from this study support this concern over large errors being introduced from the mapping algorithm. Specifically this is noticeable for pipe bomb PB1, PB2, PB4 and PB10 which were similar experiments. In fact PB1, PB2 and PB4, PB10 were intended to be repeats. Table 17 shows the error between the experiments and simulations of these repeats. This shows that the simulations have larger error between the repeated specimens than the repeated experiments. For these simulations, the only input that is different are the boundary conditions with the most notable difference being the input to the temperature mapping algorithm. The fact that the simulations show more spread between the repeats suggests that the temperature algorithm could be contributing significantly to the error. As a result, we recommend updating the temperature mapping scheme by calibrating a thermal model of the test setup including convection to all available data sets. The results from this thermal model could then be used to apply the temperatures to the mechanical model. A similar approach has been used recently for thermo-mechanical models simulating case disassembly. [6, 3]

- Even though we believe the material model was not a large source of error, improvements to the calibration could be made. Primarily, model form error for the low-rate,

Table 17: Comparisons of repeated specimen experiments and simulations. Data marked with '*' lost thermocouples before failure.

Reference Specimen	**Comparison Specimen**	**Failure Pressure Error (%)**	**Failure Temperature Error (%)**
PB1 experiment	PB2 experiment	-3.1	-1.4
PB1 simulation	PB2 simulation	6.2	-4.6
PB4 experiment	PB10 experiment	-1.3	-5.8*
PB4 simulation	PB10 simulation	7.3	-6.8

high-temperature specimens may be improved by incorporating misorientation hardening into the calibrations. Also, all the new experimental data should be explicitly incorporated into the calibration objective function. This includes the new low-rate and high-rate data, and the tension specimen profiles that were measured for some of these specimens. Adding this data to the calibration would provide the best calibration for BCJ's static recovery terms.

Although only minor improvements were made to the nominal predictions of the pipe bomb failure pressures, we believe we accurately identified the remaining sources of error in the simulations. Specifically, the temperature mapping algorithm and the geometry are believed to be the primary contributors to the errors. As a result, future work should focus on improving the temperature mapping algorithm and consider using temperature fields determined by a calibrated thermal model that includes convection. Additionally, CT scans of remaining portions of the pipe bomb material inner diameter should be taken to further understand the variability this unmachined surface introduced to the pipe bomb specimens.

References

[1] B. M. Adams, L. E. Bauman, W. J. Bohnhoff, K. R. Dalbey, M. S. Ebeida, J. P. Eddy, M. S. Eldred, P. D. Hough, K. T. Hu, J. D. Jakeman, J. A. Stephens, L. P. Swiler, D. M. Vigil, and T. M. Wildey. Dakota, A Multilevel Parallel Object-Oriented Framework for Design Optimization, Parameter Estimation, Uncertainty Quantification, and Sensitivity Analysis: Version 6.8 User's Manual. SAND Report SAND2014-4633, Sandia National Laboratories, Albuquerque, NM and Livermore, CA, 2018.

[2] B.A. Cheadle, S.A. Aldridge, and C.E. Ells. Development of texture and structure in zr-2.5 wt% nb extruded tubes. *Canadian Metallurgical Quarterly*, 11(1):121–127, 1972.

[3] B. C. Collins, J. J. Dike, K. S. Chen, and R. D. Teeter. (U) Efforts on Validating the B83 Mechanical Model: ASC V&V FY15 Project Update. SAND Report SAND2015-7984, Sandia National Laboratories, Albuquerque, NM and Livermore, CA, 2015.

[4] L.H. de Almeida, I. Le May, and P.R.O. Emygdio. Mechanistic modeling of dynamic strain aging in austenitic stainless steels. *Materials Characterization*, 41(4):137 – 150, 1998.

[5] R. de Borst. Damage, material instabilities, and failure. In E. Stein, R. de Borst, and T.J.R. Hughes, editors, *Encyclopedia of Computational Mechanics*. John Wiley & Sons, Ltd., New York, 2004.

[6] J. J. Dike, M. E. Stender, B. C. Collins, and et. al. Overview of FY17 B83 ModSim Activities: Advancing Thermal Mechanical Modeling of System Response in Abnormal Thermal Environments. SAND Report SAND2017-11277, Sandia National Laboratories, Albuquerque, NM and Livermore, CA, 2017.

[7] B. Efron. Bootstrap methods: Another look at the jacknife. *The Annals of Statistics*, 7(1):1 – 26, 1979.

[8] R. Hill. A theory of the yielding and plastic flow of anisotropic metals. *Proceedings of the Royal Society of London*, A193:281–297, 1948.

[9] Eric Jones, Travis Oliphant, Pearu Peterson, et al. SciPy: Open source scientific tools for Python, 2001–. [Online; accessed December 10, 2018].

[10] K. N. Karlson. Matcal - material model calibration tool, 2012–. [Online; accessed December 10, 2018].

[11] Hans Nordberg. Note on the sensitivity of stainless steels to strain rate. Research Report 04.0-1, AvestaPolarit Research Foundation and Sheffield Hallam University, 2004.

[12] P. J. Roache. Perspective: A method for uniform reporting of grid refinement studies. *Journal of Fluids Engineering*, 116:405 – 413, 1994.

[13] Vicente Romero, J. Franklin Dempsey, and Bonnie Antoun. Case Study Example: Application of UQ and V&V to Experiments and Simulations of Heated Pipes Pressurized to Failure. SAND Report SAND2014-4870P, Sandia National Laboratories, Albuquerque, NM and Livermore, CA, 2014.

[14] Vicente Romero, J. Franklin Dempsey, and Bonnie Antoun. UQ and V&V Techniques applied to Experiments and Simulations of Heated Pipes Pressurized to Failure. SAND Report SAND2014-3985, Sandia National Laboratories, Albuquerque, NM and Livermore, CA, 2014.

[15] William Scherzinger. Pressurization of a Ring in Plane Strain. SAND Report SAND2013-5457P, Sandia National Laboratories, Albuquerque, NM and Livermore, CA, 2013.

[16] SIERRA Solid Mechanics Team Team. Sierra/SolidMechanics 4.48 User's Guide. SAND Report SAND2018-2961, Sandia National Laboratories, Albuquerque, NM and Livermore, CA, 2018.

[17] S. Ukai, M. Harada, H. Okada, M. Inoue, S. Nomura, S. Shikakura, T. Nishida, M. Fujiwara, and K. Asabe. Tube manufacturing and mechanical properties of oxide dispersion strengthened ferritic steel. *Journal of Nuclear Materials*, 204:74 – 80, 1993.

[18] Z. Yanushkevich, A. Mogucheva, M. Tikhonova, A. Belyakov, and R. Kaibyshev. Structural strengthening of an austenitic stainless steel subjected to warm-to-hot working. *Materials Characterization*, 62(4):432 – 437, 2011.

A Parameter Histogram and Q-Q Plots

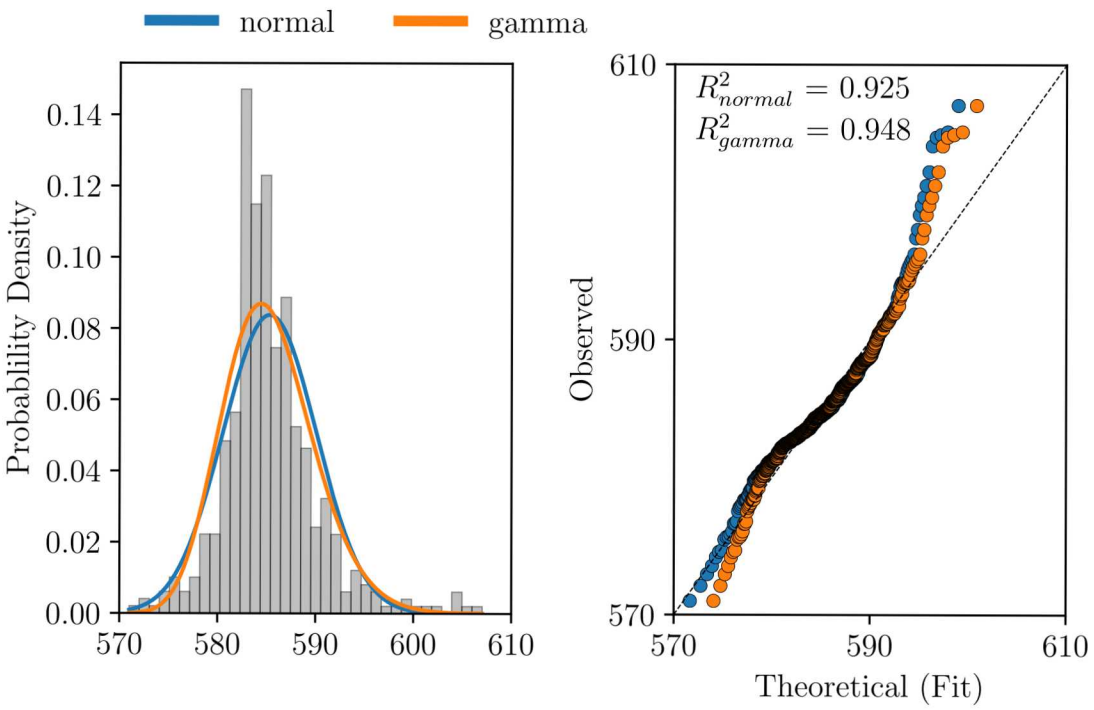

Figure A.1: Histogram and Q-Q plots for Y_0

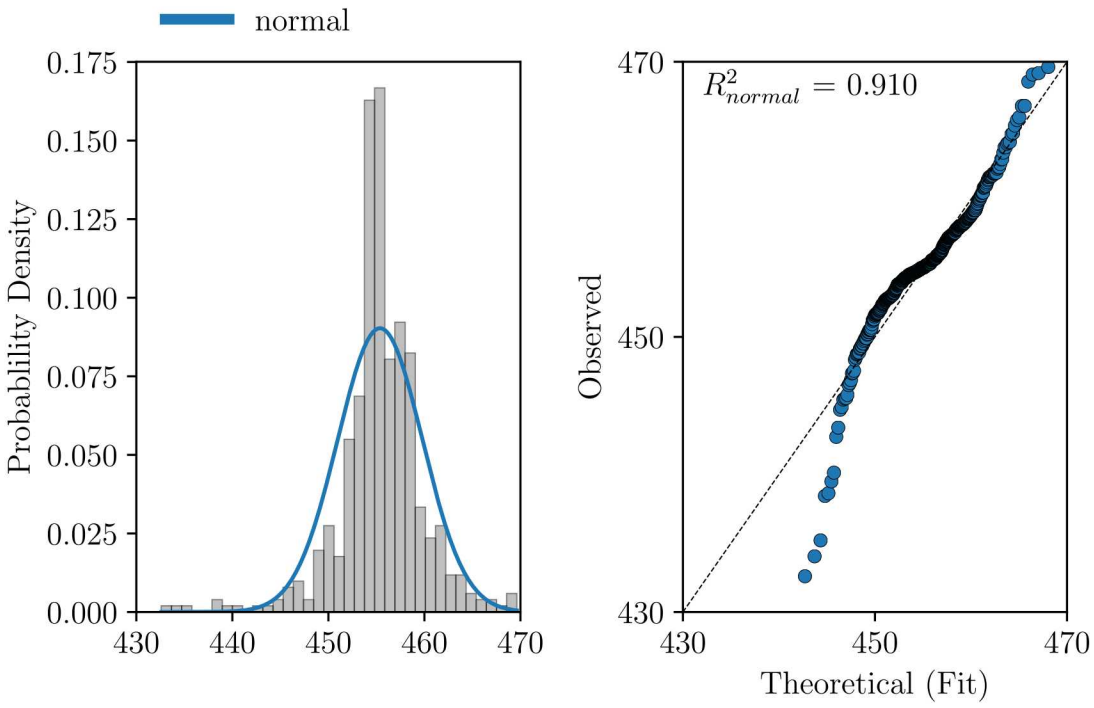

Figure A.2: Histogram and Q-Q plots for Y_1

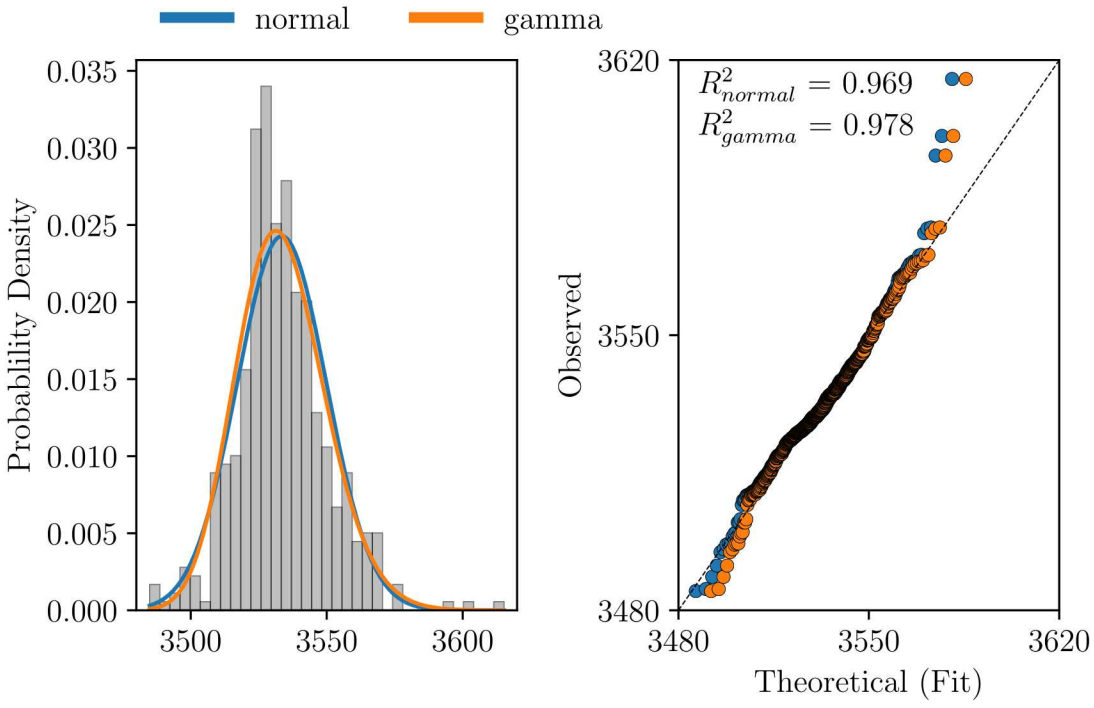

Figure A.3: Histogram and Q-Q plots for H

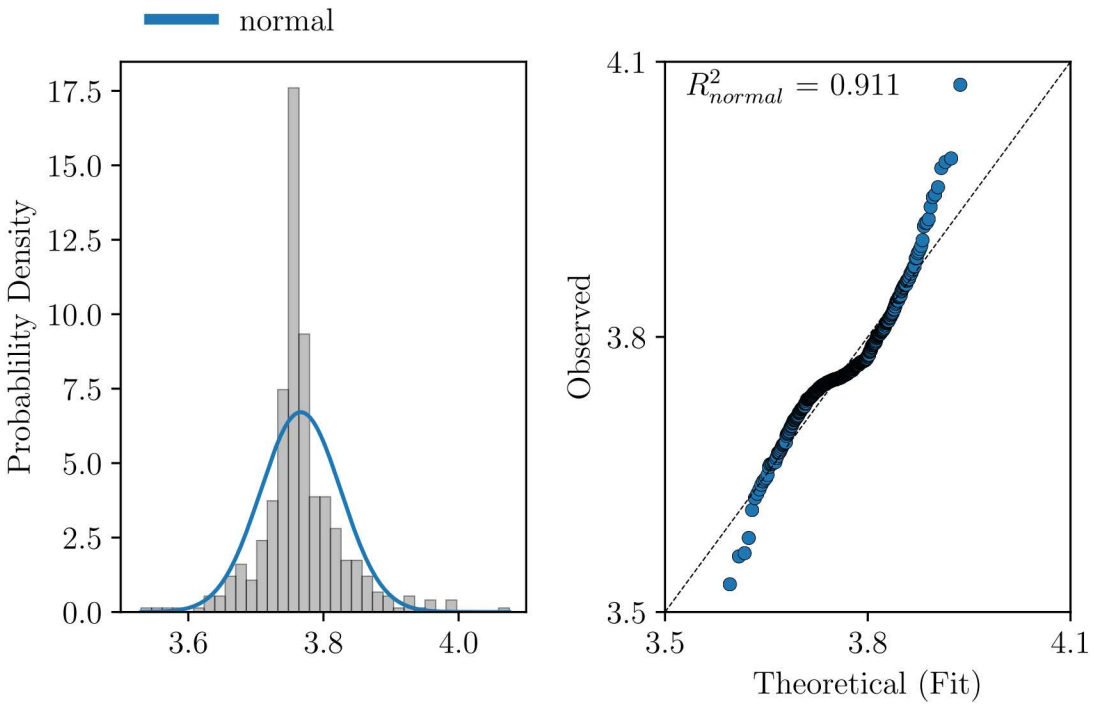

Figure A.4: Histogram and Q-Q plots for R_d^{296}

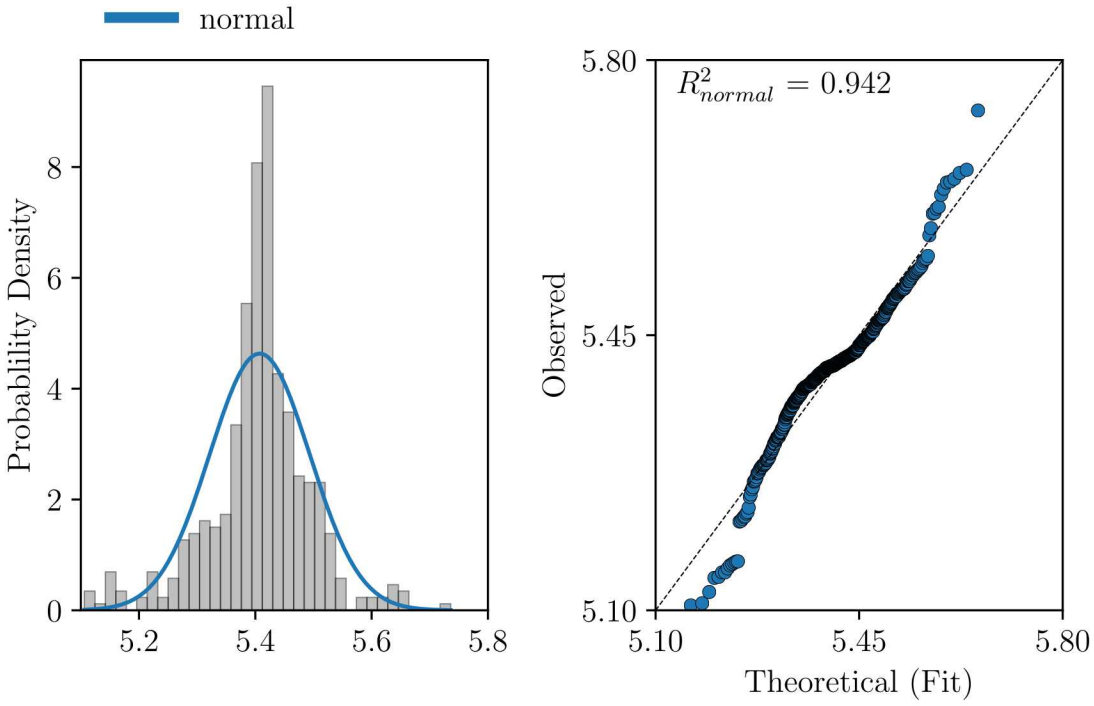

Figure A.5: Histogram and Q-Q plots for R_d^{373}

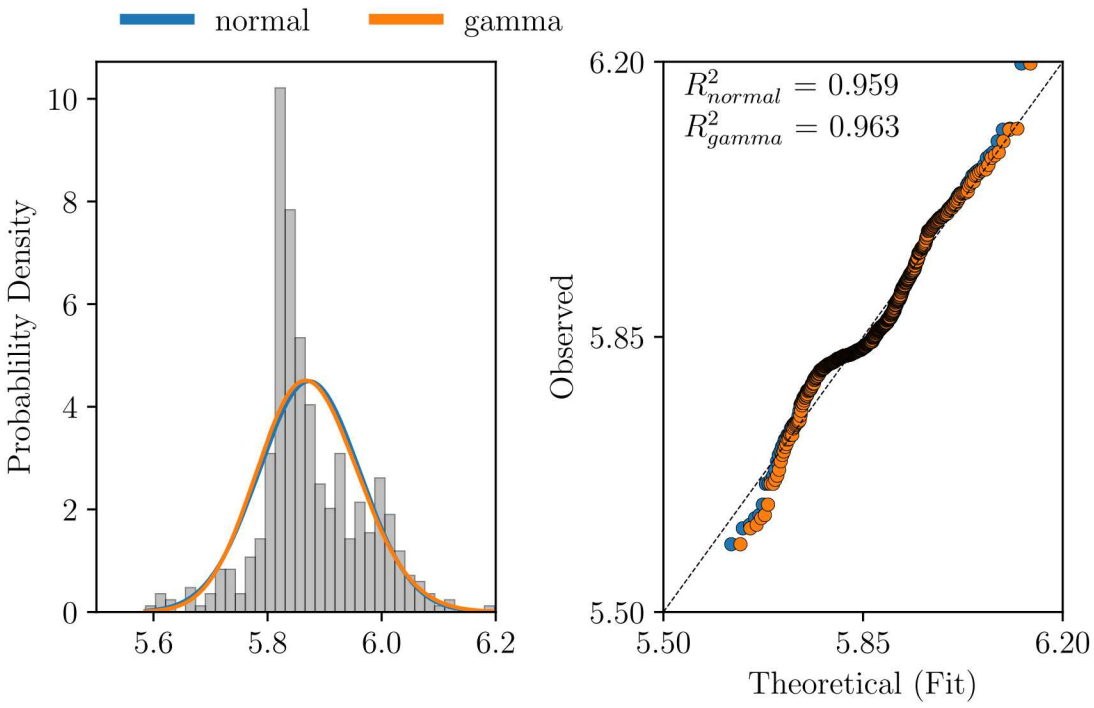

Figure A.6: Histogram and Q-Q plots for R_d^{473}

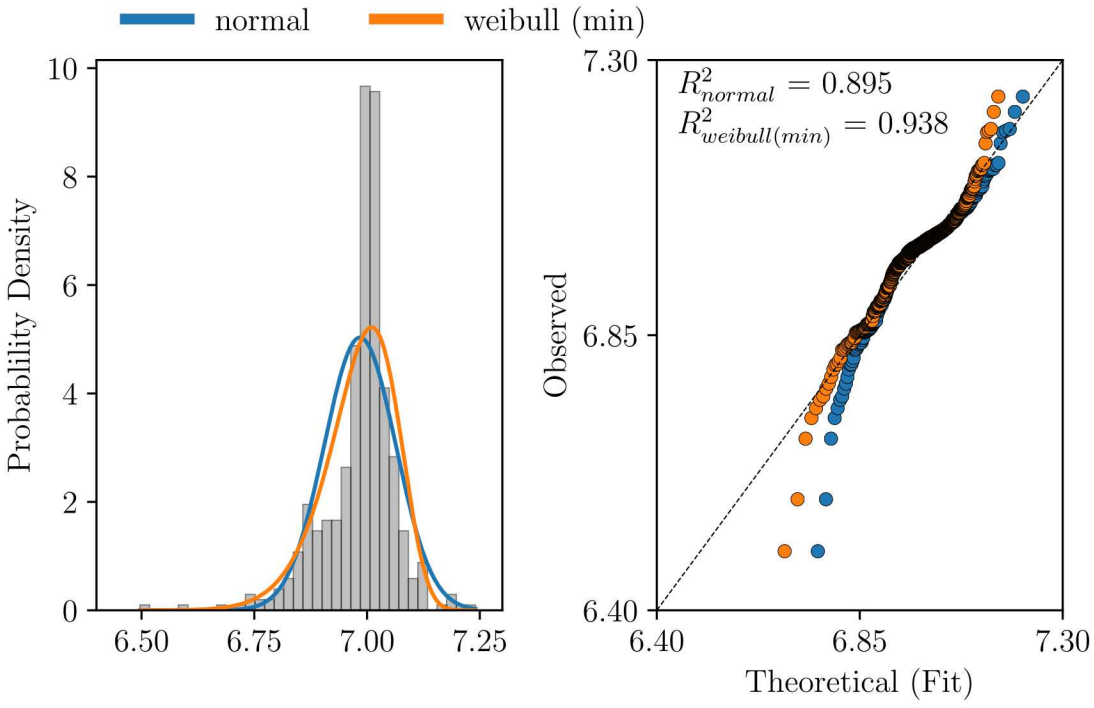

Figure A.7: Histogram and Q-Q plots for R_d^{673}

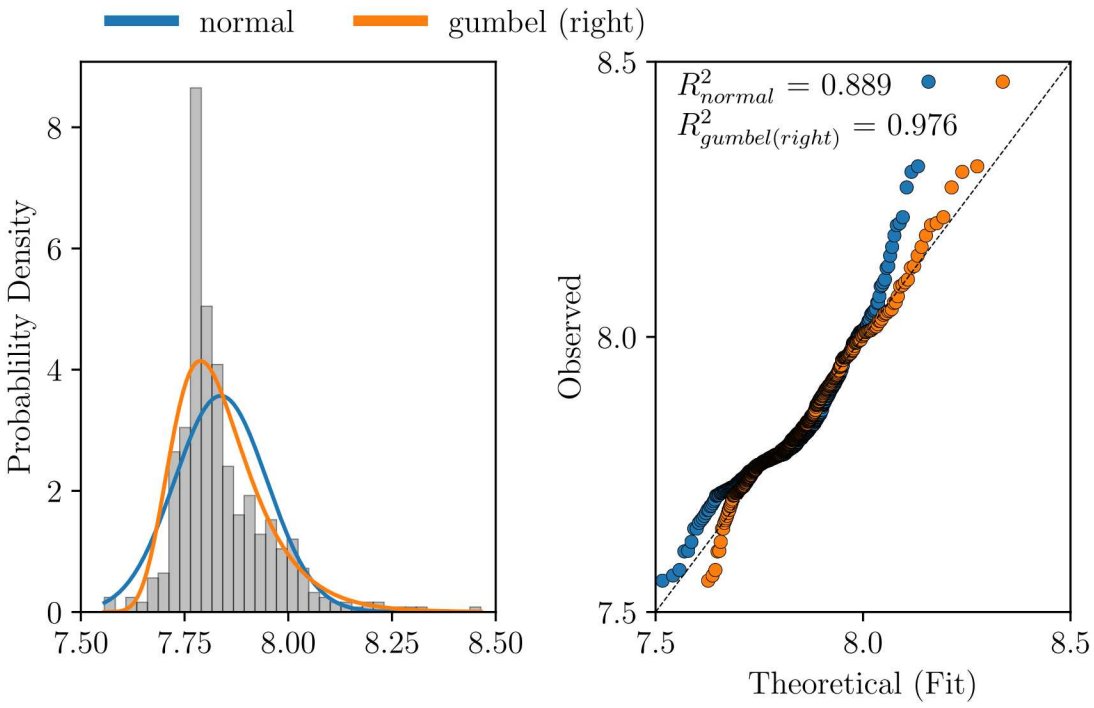

Figure A.8: Histogram and Q-Q plots for R_d^{873}

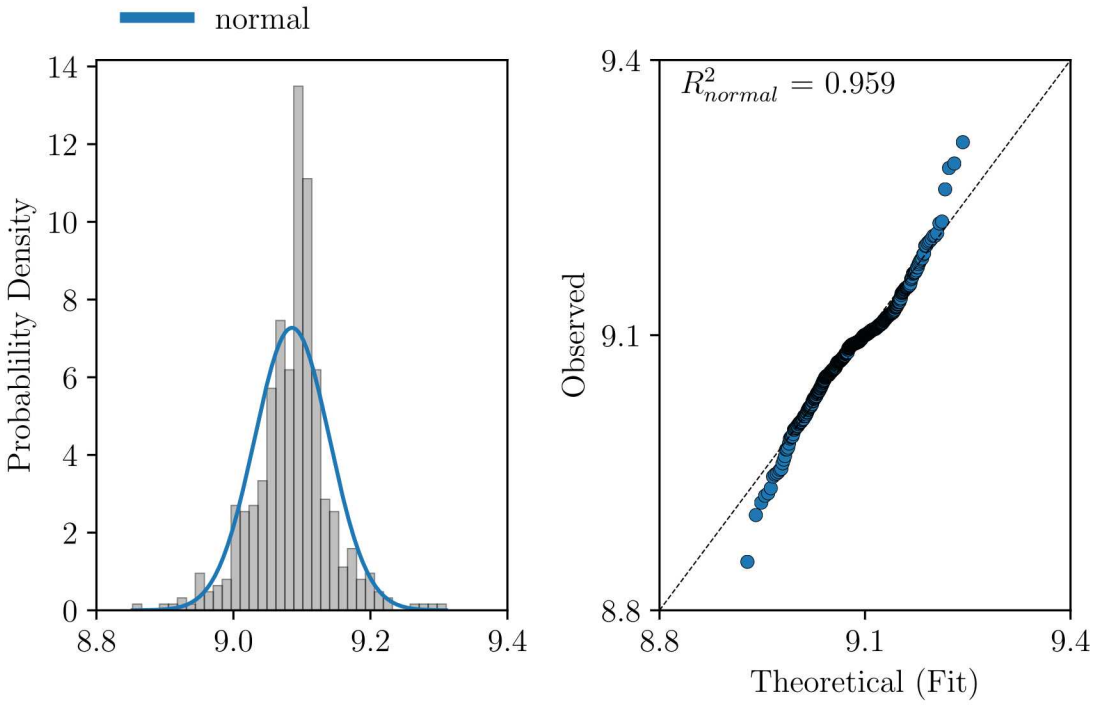

Figure A.9: Histogram and Q-Q plots for R_d^{973}

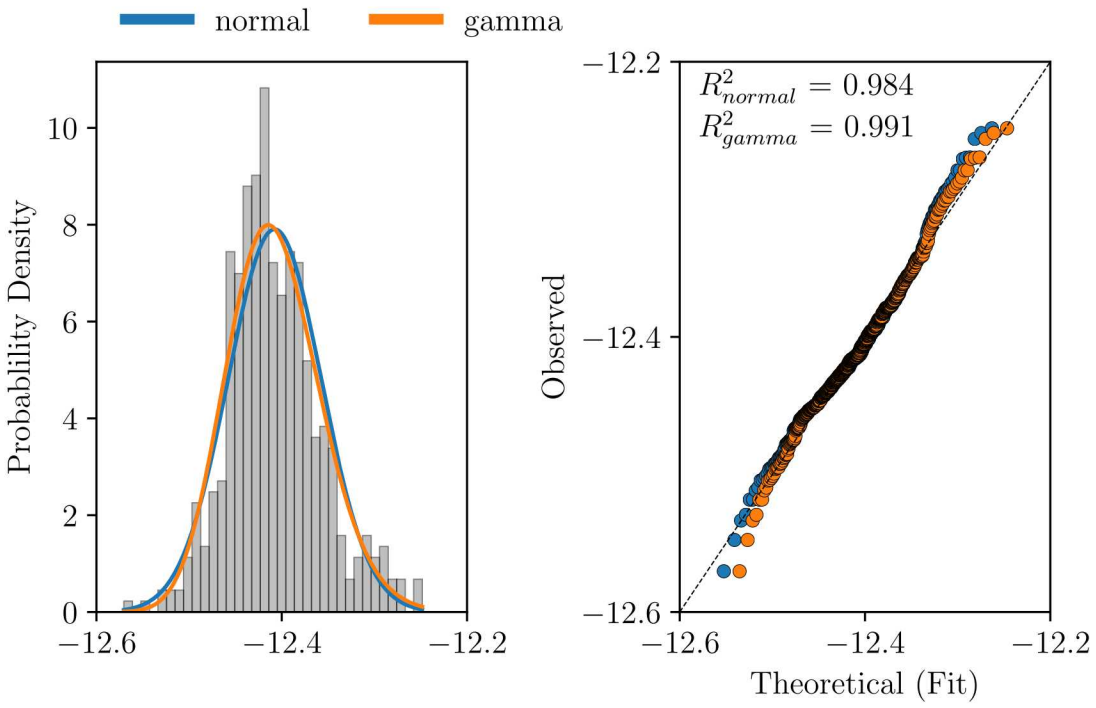

Figure A.10: Histogram and Q-Q plots for Q_s

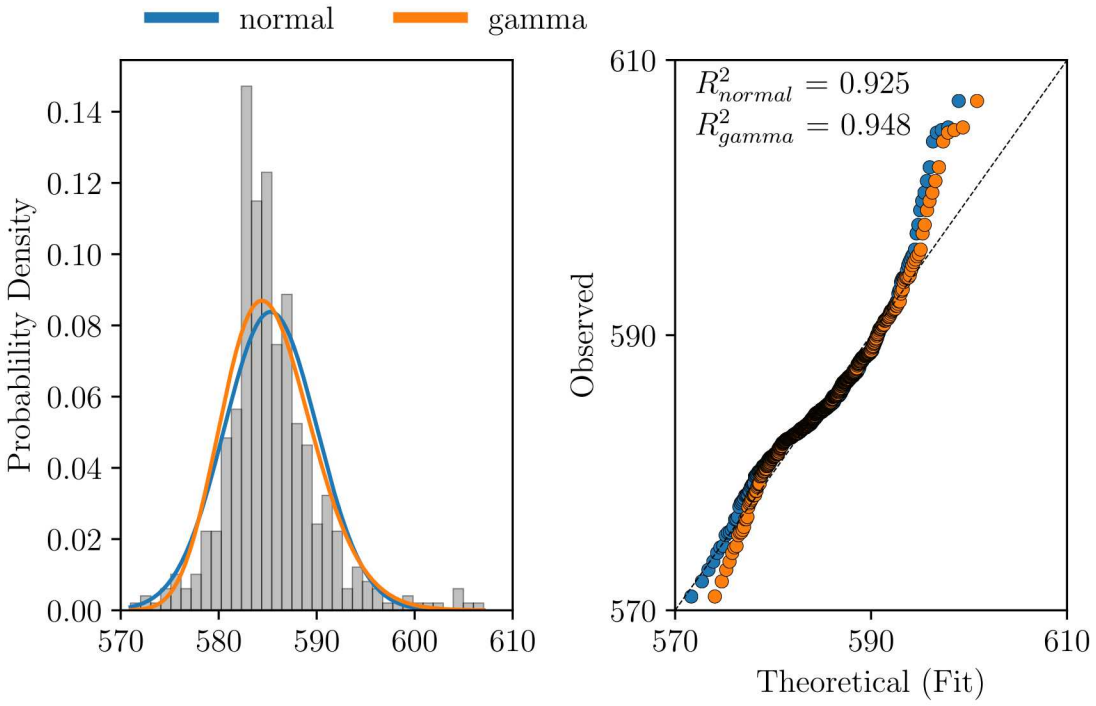

Figure A.11: Histogram and Q-Q plots for R_s

B Final Element Plastic Strain and Temperature Histograms for all Nominal Pipe Bomb Simulations

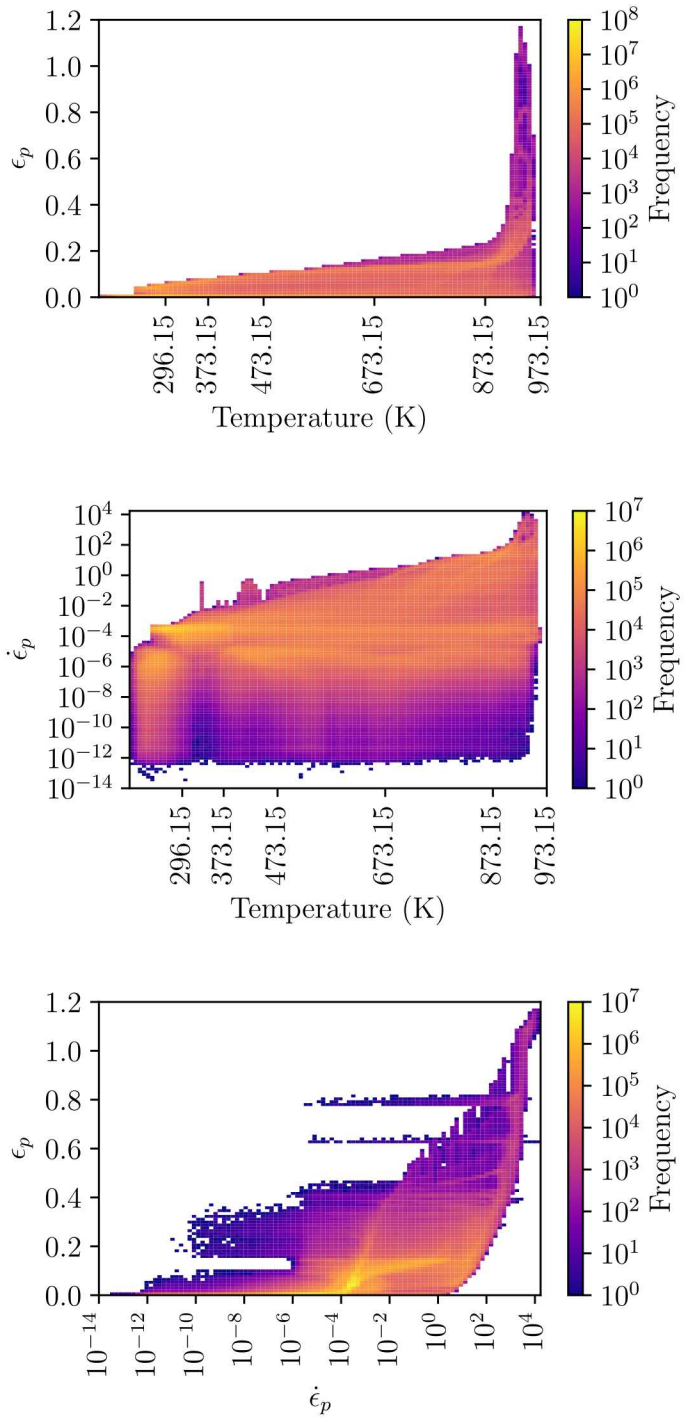

Figure B.12: Temperature, ϵ_p, and $\dot{\epsilon}_p$ histograms for PB2.

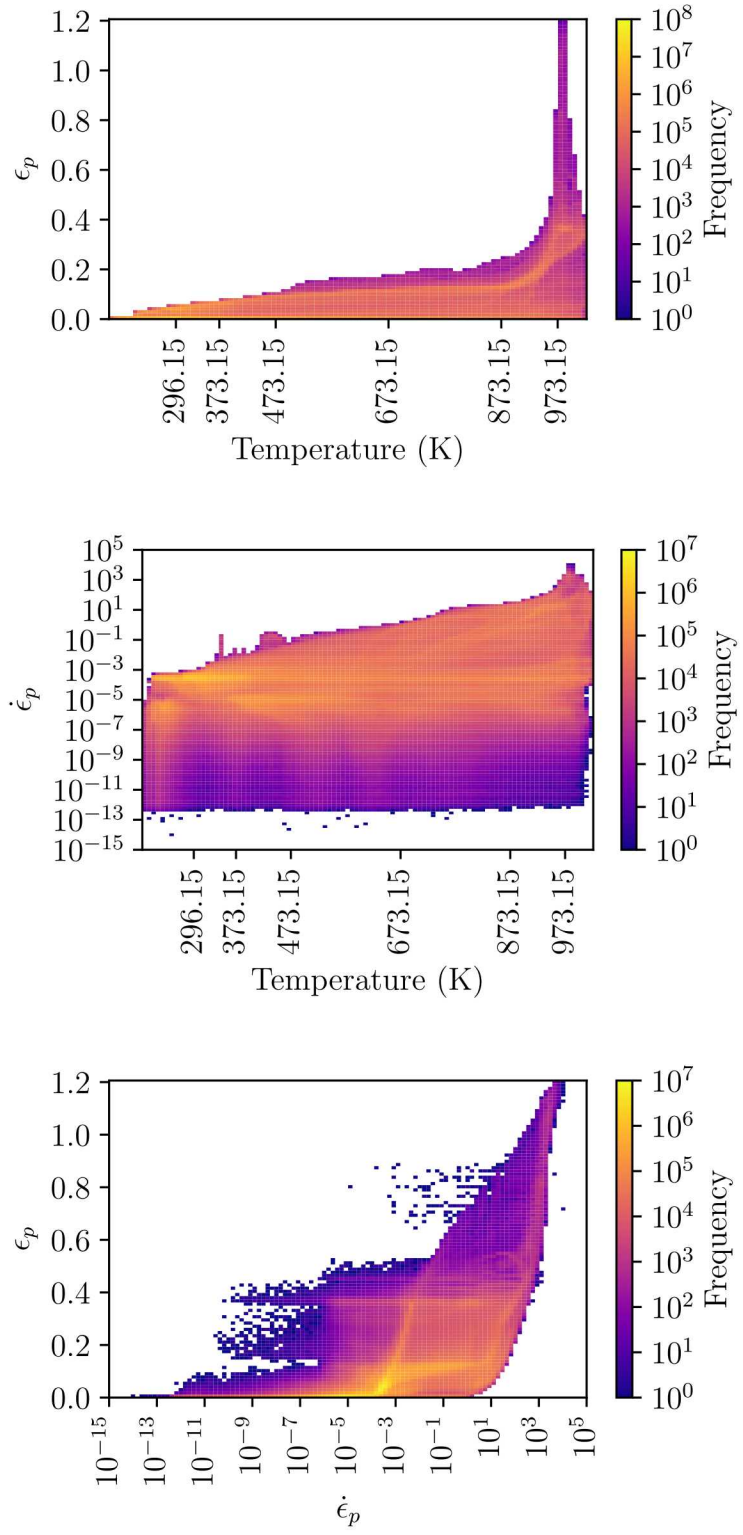

Figure B.13: Temperature, ϵ_p, and $\dot{\epsilon}_p$ histograms for PB4.

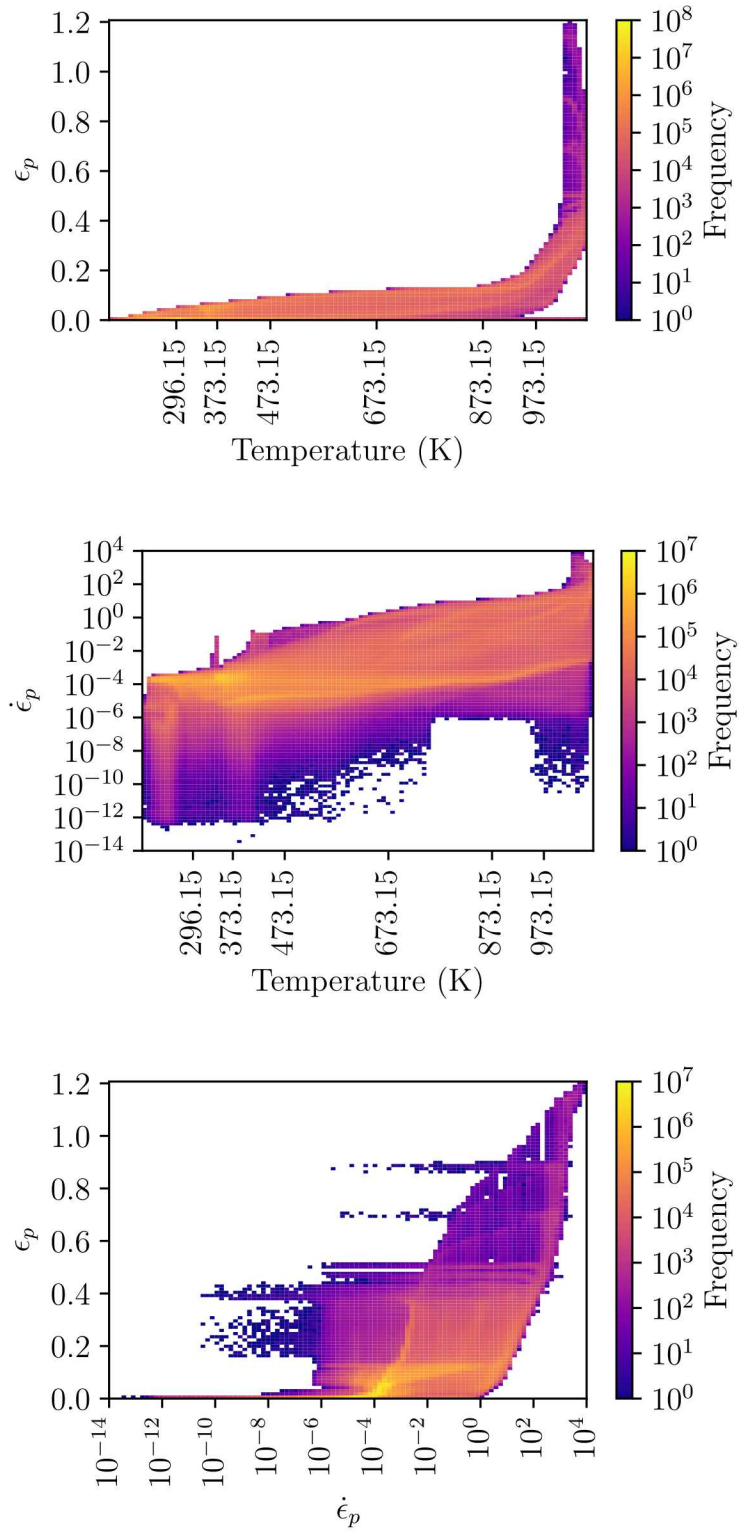

Figure B.14: Temperature, ϵ_p, and $\dot{\epsilon}_p$ histograms for PB8.

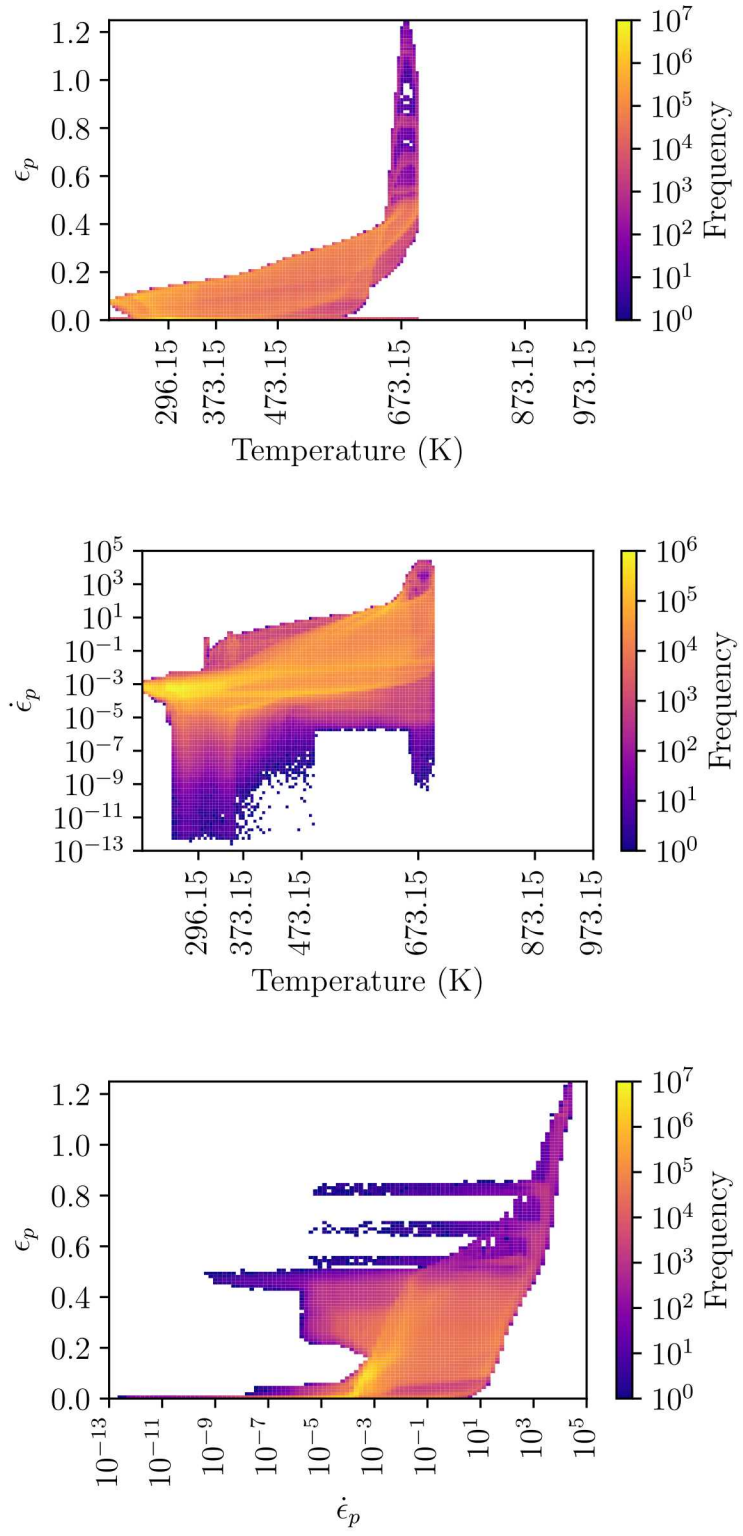

Figure B.15: Temperature, ϵ_p, and $\dot{\epsilon}_p$ histograms for PB9.

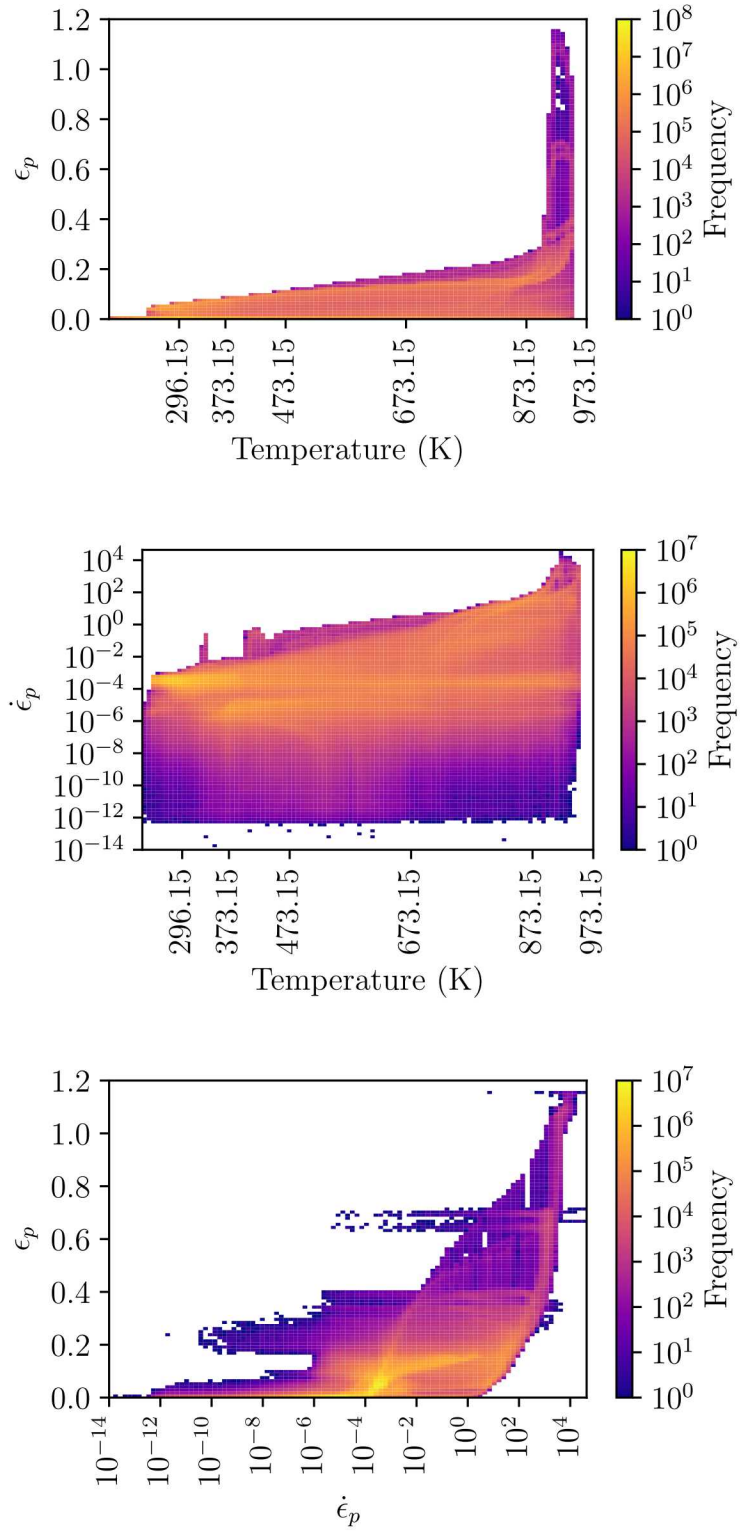

Figure B.16: Temperature, ϵ_p, and $\dot{\epsilon}_p$ histograms for PB10.

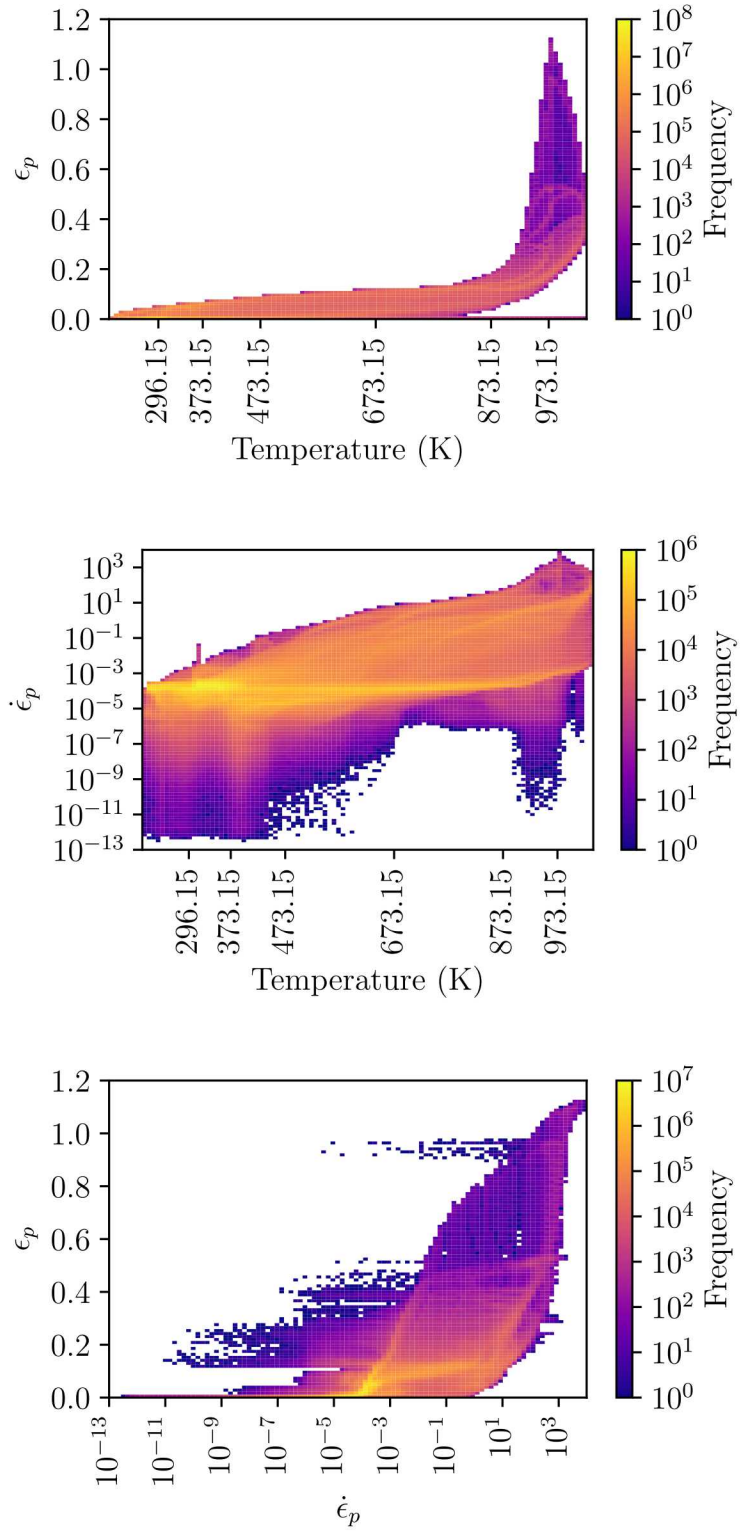

Figure B.17: Temperature, ϵ_p, and $\dot{\epsilon}_p$ histograms for PB15.

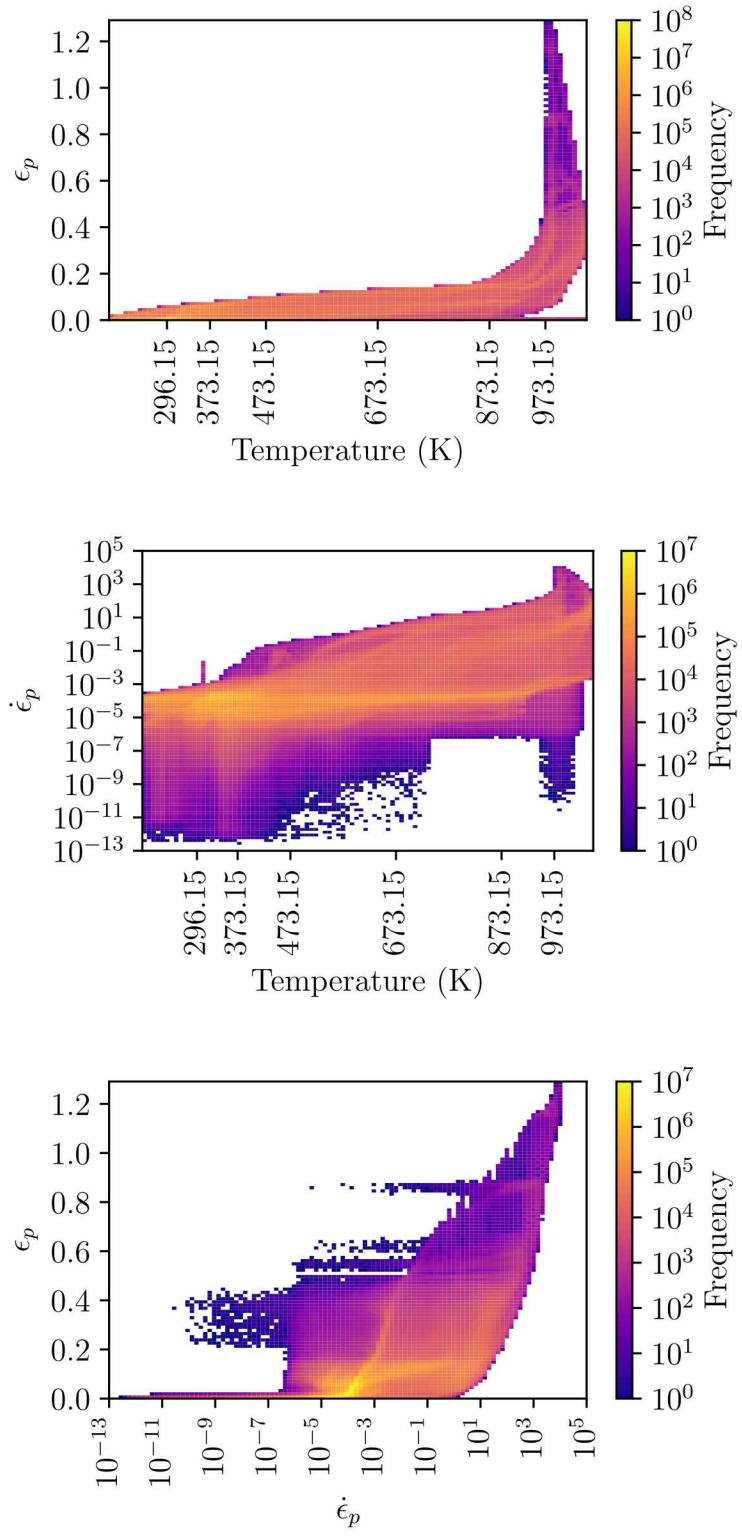

Figure B.18: Temperature, ϵ_p, and $\dot{\epsilon}_p$ histograms for PB16.

C SierraSM Material Model Files

C.1 Calibrated Material Model from SOGA Calibration

```
# Units N, m, Pa, s, K

  begin definition for function thermal_strain
    type is piecewise linear
    begin values
       218.0  -0.001264
       293.0   0.0
       373.0   0.001348
       473.0   0.003107
       573.0   0.004934
       673.0   0.006840
       773.0   0.008832
       873.0   0.010846
      1293     0.019305
    end
  end

  begin definition for function youngs_modulus_multiplier
    type is piecewise linear
    begin values
       294.11    1.0
      1673.0     0.4
    end
  end

  begin definition for function poissons_ratio_multiplier
    type is piecewise linear
    begin values
       294.11    1.0
      1673.0     1.49
    end
  end

  begin definition for function yield_function
    type is analytic
    evaluate expression = "(5.758210000000000e+02/(1 +
    6.3128093451e+00*exp(-4.7266027563e+02/x)))*0.5*(1 + tanh(10^-2.734364062*(1453.4900336 - x)));"
  end

begin definition for function dynamic_recovery_function
  type is piecewise linear
  begin values
     296.15  3.965310000000000e+00
     373.15  4.191960000000000e+00
     473.15  5.896409999999999e+00
     673.15  6.755130000000000e+00
     873.15  7.751420000000000e+00
     973.15  9.090070000000001e+00
```

```
  end values
end definition for function dynamic_recovery_function


  begin definition for function rs_function
    type is piecewise linear
    begin values
       296.15  0
       373.15  0
       473.15  0
       673.15  0
       873.15  0
#    873.15   33.333333
#Updated value for slow-rate 600C experiments,
#not used for FY18 Pipe Bomb Sand Report, may need a little work
       973.15  5.375967500000000e+01
    end
  end

  begin definition for function qs_function
    type is piecewise linear
    begin values
       296.15  0
       373.15  0
       473.15  0
       673.15  0
       873.15  0
#    873.15   2.410009497e-15
#Updated value for slow-rate 600C experiments,
#not used for FY18 Pipe Bomb Sand Report, may need a little work.
       973.15  {10^-1.246775000000000e+01}
    end
  end


  begin property specification for material pb_304L
    density = 7609
    thermal engineering strain function = thermal_strain

    begin parameters for model elastic
      youngs modulus = 200e+09
      poissons ratio = 0.27
    end

    begin parameters for model dsa
      flow_rule = evp

      youngs modulus = 200e+09
      youngs modulus function = youngs_modulus_multiplier

      poissons ratio = 0.27
      poissons ratio function = poissons_ratio_multiplier

      rate independent yield constant =  1.0e+06
```

```
    initial yield function = yield_function

    isotropic hardening constant = {3.526220000000000e+03*1.0e+06}

    isotropic dynamic recovery constant = 1
    dynamic recovery function = dynamic_recovery_function


    flow rule coefficient constant =  {10^4.57448468538}
    flow rule exponent constant =     3.56763776501

    hardening_rate dependence coefficient constant =  0.0
    hardening_rate dependence exponent constant = 0.0

    isotropic static recovery constant = 1.0
    static_recovery_rs_function = rs_function

    isotropic static recovery sinh constant = 1.0
    static_recovery_qs_function = qs_function

    temperature option = 0.0  # (0.0 = driven externally, 1.0 = uncoupled adaibatic heating)
    plastic dissipation factor = 0.8 #  fraction of plastic work that is dissipated as heat

   # Only used for uncoupled adiabatic heating
    density for plastic dissipation calculations = 7609
    specific heat for plastic dissipation calculations = 500
    initial temperature for uncoupled adiabatic heating = 296

    semi implicit plastic strain solver number of iterations = 250
    semi implicit plastic strain solver residual tolerance = 1e-14

    initial damage = 1e-4
    maximum damage = 0.5
    damage exponent = 3.5

    initial void size = 2
    initial void count per volume = 5e-5
    nucleation parameter1 = 0.0
    nucleation parameter2 = 0.0
    nucleation parameter3 = 0.0
    nucleation parameter4 = 1.0

    maximum change in damage allowed per timestep = 0.1
    implicit damage solver number of iterations = 100
    implicit damage solver residual tolerance = 1.0e-9
   end
  end
 end
```

C.2 Hill Material Model

The isotropic version of this material model has $R_{22} = 1$ while the material models with a 5% and 10% reduction in the hoop direction yield have $R_{22} = 0.95$ and $R_{22} = 0.9$, respectively.

The material model with a the 5% reduction in the hoop direction yield is included here.

```
# units: N, m, Pa, K, s

### FUNCTION DEFINITIONS ###########################################################

## Thermal Strain ##
  begin definition for function thermal_strain
    type is piecewise linear
    begin values
       218.0  -0.001264 ## (m/m/K)
       293.0   0.0
       373.0   0.001348
       473.0   0.003107
       573.0   0.004934
       673.0   0.006840
       773.0   0.008832
       873.0   0.010846
      1293     0.019305 # extrapolated
    end
  end

## Multiplier for E ##
  begin definition for function youngs_modulus_multiplier
    type is piecewise linear
    begin values
       294.11    1.0  ##(.)
      1673.0     0.4
    end
  end

## Multiplier for nu ##
  begin definition for function poissons_ratio_multiplier
    type is piecewise linear
    begin values
       294.11    1.0  ##(.)
      1673.0     1.49
    end
  end

## Yield ##
  begin definition for function yield_function
    type is analytic
    evaluate expression = "(5.758210000000000e+02/(1 +
    6.3128093451e+00*exp(-4.7266027563e+02/x)))*0.5*(1 + tanh(10^-2.734364062*(1453.4900336 - x)));"
  end

### Material Coordinate System

Begin Coordinate System CSYSCYL
  Type = cylindrical
  origin = o
```

```
  vector = z
  point = cyl_x
End


### PHYSICAL PROPERTY DEFINITIONS ################################################

  begin property specification for material pb_304L
    density = 7609  ##(kg/m^3)
    thermal engineering strain function = thermal_strain

  ## Elastic Model ##
    begin parameters for model elastic
      youngs modulus = 200e+09  ##(Pa)
      poissons ratio = 0.27    ##(.)
    end

    begin parameters for model hill_plasticity_damage
      youngs modulus                = 200e9
      poissons ratio                =   0.27
      yield stress                  =   1.0e+06
      r11                           =   1
      r22                           =   0.95
      r33                           =   1
      r12                           =   1
      r23                           =   1
      r31                           =   1

      hardening model = decoupled_flow_stress
      isotropic hardening model = voce

      hardening modulus  = {3.526220000000000e+03*1.0e+06/8.42071}
      exponential coefficient = 8.42071

      yield rate multiplier = power_law_breakdown
      yield rate coefficient = {10^4.57448468538}
      yield rate exponent =    3.56763776501

      hardening rate multiplier = rate_independent

      yield temperature multiplier = user_defined
      yield temperature multiplier function = yield_function

      hardening temperature multiplier = temperature_independent

      coordinate system             = CSYSCYL
      direction for rotation        = 1
      alpha                         = 0.0
      second direction for rotation = 2
      second alpha                          = 0.0

      max_ls_iter = 1e3
      max_rma_iter = 1e3
```

```
    # Damage parameters --- Generic and Uncalibrated
    initial damage = 1e-4
    maximum damage = 0.5
    damage exponent = 3.5

    initial void size = 2e-5
    initial void count per volume = 5
    nucleation parameter 1 = 0
    nucleation parameter 2 = 0
    nucleation parameter 3 = 0
    nucleation parameter 4 = 1.0

    IMPLICIT DAMAGE SOLVER NUMBER OF ITERATIONS = 55.0
    IMPLICIT DAMAGE SOLVER RESIDUAL TOLERANCE = 1.e-10
  end
end
```


Sandia National Laboratories